Rare mutations implicate CGE interneurons as a vulnerable axis of cognitive deficits across psychiatric disorders

Stephanie A. Herrlinger[1,2]*, Jiayao Wang[3]*, Bovey Y Rao[1,2,4], Jonathan Chang[3], Joseph A. Gogos [1,2,5,6,7]†, Attila Losonczy[1,2]† and Dennis Vitkup[3]†

[1] Department of Neuroscience, Columbia University, New York, NY, United States
[2] Mortimer B. Zuckerman Mind Brain Behavior Institute, Columbia University, New York, NY, United States
[3] Department of Systems Biology and Department Biomedical Informatics, Columbia University, New York, NY, United States
[4] Doctoral Program in Neurobiology and Behavior, Columbia University, New York, NY, United States
[5] Department of Physiology, Columbia University, New York, NY, United States
[6] Department of Psychiatry, Columbia University, New York, NY, United States
[7] Stavros Niarchos Foundation Center for Precision Psychiatry and Mental Health, Columbia University, New York, NY, United States
*These authors contributed equally to this work
† Correspondence should be addressed to JG (jag90@columbia.edu), AL (al2856@columbia.edu) and DV (dv2121@cumc.columbia.edu)

Abstract

Neuropsychiatric disorders such as autism spectrum disorder (ASD) and schizophrenia (SCZ) share genetic risk factors, including rare high penetrance single nucleotide variants and copy number variants (CNVs), and exhibit both overlapping and distinct clinical phenotypes. Cognitive deficits and intellectual disability—critical predictors of long-term outcomes—are common to both conditions. To investigate shared and disorder-specific neurobiological impact of highly penetrant rare mutations in ASD and SCZ, we analyzed human single-nucleus whole-brain sequencing data to identify strongly affected brain cell types. Our analysis revealed Caudal Ganglionic Eminence (CGE)-derived GABAergic interneurons as a key nexus for cognitive deficits across these disorders. Notably, genes within 22q11.2 deletions, known to confer a high risk of SCZ, ASD, and cognitive impairment, showed a strong expression bias toward vasoactive intestinal peptide-expressing cells (VIP+) among CGE subtypes. To explore VIP+ GABAergic interneuron perturbations in the 22q11.2 deletion syndrome *in vivo*, we examined their activity in the *Df(16)A*$^{+/-}$ mouse model during a spatial navigation task and observed reduced activity along with altered responses to random rewards. At the population level, VIP+ interneurons exhibited impaired spatial encoding and diminished subtype-specific activity suggesting deficient disinhibition in CA1 microcircuits in the hippocampus, a region essential for learning and memory. Overall, these results demonstrate the crucial role of CGE-derived interneurons in mediating cognitive processes that are disrupted across a range of psychiatric and neurodevelopmental disorders.

Introduction

Psychiatric disorders exhibit distinct clinical symptoms yet frequently share genetic risk factors and underlying cellular and molecular mechanisms[1–6]. For example, schizophrenia (SCZ) is characterized by psychosis, including hallucinations and delusions, as well as cognitive control impairments leading to disorganization, impulsivity, and difficulties in working memory. In contrast, autism spectrum disorder (ASD) is characterized by restricted interests and heightened anxiety, along with cognitive rigidity and repetitive behaviors[7,8]. Several copy number variations (CNVs), such as the 22q11.2 deletion, have been implicated in both SCZ and ASD, as well as in other psychiatric disorders[9,10]. Among their diverse symptoms, cognitive impairments and intellectual disability (ID), which are frequently comorbid with neuropsychiatric phenotypes[11] and are especially pronounced in cases with high genetic risks[11–14]. Cognitive deficits in psychiatric disorders are particularly debilitating, as their severity strongly predicts long-term health deficits and well-being outcomes[15–17]. These deficits encompass a broad range of functions including memory, attention, reasoning, decision-making and social cognition[18].

Despite advances in genetic research on disorders such as ASD and SCZ[1,2,19], therapeutic progress in treating cognitive symptoms remains limited, largely due to gaps in understanding the neurobiological mechanisms through which genetic risk factors impact cognition. To better understand the relationships between genetics and psychiatric phenotypes, researchers are increasingly integrating genetic analyses with single-cell and single-nucleus sequencing data to identify cell types affected across psychiatric disorders[20–22]. Animal models, particularly mouse models that replicate rare high-risk genetic insults, play a critical role in this integrative approach. The evolutionary conservation of brain regions, cell types, and core biological processes between mice and humans[23–26] facilitates detailed examination of genetic risk factors at both cellular and circuit levels[27–32].

In this study we investigated the collective neurobiological impact of rare, highly penetrant mutations in ASD, SCZ, and 22q11.2 deletion syndrome across diverse brain cell types, using recently released human single-nucleus whole-brain RNA sequencing data[33] (Fig. 1). Our analyses revealed distinct disorder-specific mutation biases affecting different cell types, with caudal ganglionic eminence (CGE)-derived interneurons consistently implicated across genetic insults associated with cognitive dysfunction, including ASD with intellectual disability, SCZ, and Developmental Disorders and Intellectual Disability (DD/ID). Furthermore, our analysis of genes within the 22q11.2 deletion revealed that VIP+ CGE-derived interneurons were strongly affected in this condition. Using *in vivo* two-photon calcium imaging of VIP+ GABAergic interneuron activity in a mouse model of 22q11.2 deletion, we observed specific alterations in interneuron-selective interneuron (ISI) cell types, which primarily inhibit other interneurons. These findings implicate ISI dysfunction in circuit-level abnormalities contributing to cognitive and behavioral phenotypes characteristic of this syndrome and likely many other psychiatric conditions.

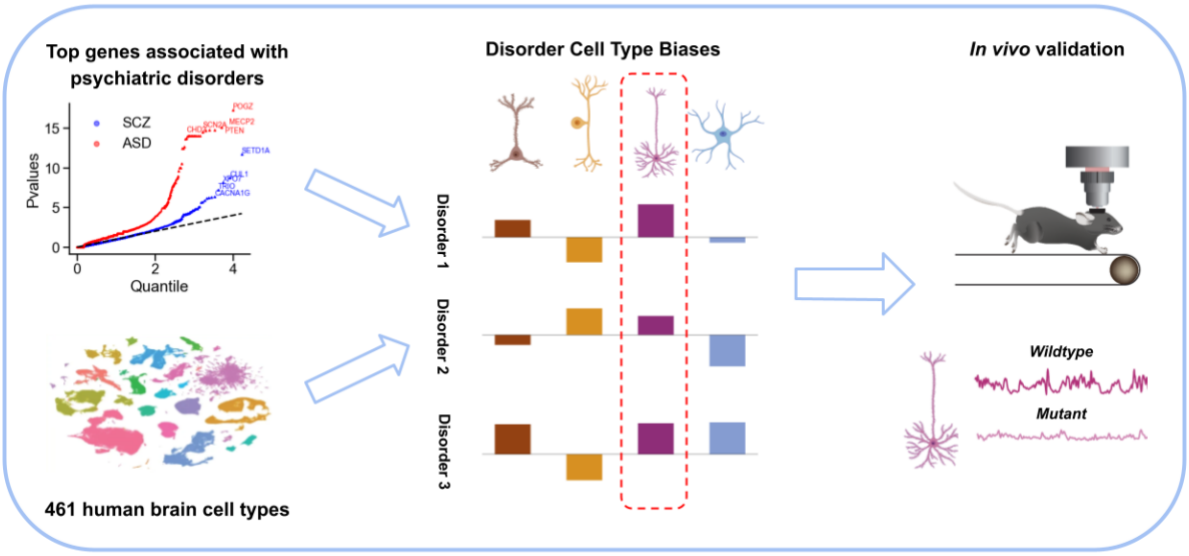

Figure 1. Overview of study methodology. Left: Integration of genetic and single-cell transcriptomic data to identify cell type-specific disorder biases. Top significant genes implicated in ASD and SCZ[1,2] and human brain snRNA-seq data were used to create cell type mutation bias analysis using 461 human brain cell types[33]. **Middle:** Disorder cell type bias analysis reveals shared cell type risk patterns between distinct disorders with overlapping cognitive phenotypes. **Right:** Experimental validation in a relevant mouse model allows us to describe identified cell type specific deficits *in vivo* using 2-photon calcium imaging to capture neuronal activity during behavior.

Results

Identifying disorder cell type mutation bias leveraging rare variants and snRNA-seq data

In our study we focused on rare mutations, which individually typically have substantially higher functional impacts on psychiatric phenotypes compared to common variants[1,34]. The availability of comparably-sized, well-characterized rare variant datasets from both ASD and SCZ cohorts enabled us to perform direct cross-disorder comparisons. For ASD, we utilized a recent meta-analysis performed by the SPARK consortium[2], which comprised *de novo* mutations from 42,607 ASD probands. This analysis identified 61 genes with exome-wide significance. For schizophrenia, we used a case-control study involving 24,248 schizophrenia patients and 97,322 control patients from the SCHEMA consortium[1]. In our main analysis, we selected the top 61 SCZ genes based on genetic association strength, to match the number of considered ASD genes.

A significant fraction of individuals in the ASD cohort exhibit low IQs (IQ ≤ 70, which we refer to as "ASD with ID")[35,36] (Suppl. Fig. 1). To facilitate a more appropriate comparison with SCZ, where the average premorbid IQ is approximately 94[37,38], we selected higher IQ (IQ >70) ASD cases from the SPARK cohort (hereafter referred to as "ASD", with the average IQ ~95). Notably, individuals with SCZ who carry rare mutations have IQ scores that are only marginally lower than those in the broader schizophrenia population[39]. Furthermore, genes implicated in higher-IQ ASD also share more similar developmental expression profiles with SCZ genes compared to genes associated with lower-IQ ASD (Suppl. Fig. 2). Even though SCZ and ASD cases have comparable overall IQs, the nature of cognitive dysfunction in these conditions is often distinct. While SCZ is usually characterized by broad deficits across multiple cognitive domains, such as working memory, processing speed, and executive function[40,41], high-functioning ASD cases tend to show more selective, domain-specific cognitive impairments, particularly in areas like social cognition and communication[42,43].

To investigate relative brain cell type impact in ASD and SCZ, we used a recent single-nucleus sequencing dataset collected from the entire human brain[33]. This dataset encompassed approximately 105 anatomical locations dissected from three different donors across the forebrain, midbrain, and hindbrain, with 3,369,219 individual nuclei that were classified into 31 superclusters and 461 distinct cell types (Fig. 1). To identify which brain cell types are most impacted by disease-causing mutations, we calculated cell-type-specific mutation biases. Our goal was to identify cell types where affected mutations showed strong expression specificity relative to other cell types, indicating their likely crucial role in the disorder's pathophysiology. To quantify the mutation biases, we first calculated the specificity of each gene's expression to a particular cell type using a Z-score (see Methods). To account for overall expression differences across different cell types, we then compared each gene's Z-score to the distribution of Z-scores for random genes with similar brain expression levels. Finally, we weighted each ASD gene by *de novo* mutation counts, and SCZ genes by their effective mutation counts in cases, due to differences in the original genetic study designs (Suppl. Fig. 3, see Methods). The mutation bias towards each cell types in ASD and SCZ was then calculated as the mutation-weighted average of expression specificities across cell types for each disorder (Suppl. Table 2, Suppl. Fig. 4). This cell-type

mutation bias thus considers both the degree to which each disease gene is specifically expressed in each cell type and the strength of its genetic contribution with the disorder.

Shared cell type vulnerability signatures across ASD and SCZ

Our analysis revealed a strong correlation between ASD and SCZ mutation biases across cell type clusters in human brain cell atlas (Fig. 2A), with cell types showing strong mutation biases in ASD also showing strongly mutation biases in SCZ (Spearman correlation = 0.66, $P<10^{-10}$). This correlation remains strong when only considering neuronal cell types, indicating that it is not simply due to a general neuronal bias in both disorders. The strong correlation is also not due to gene overlapping between ASD and SCZ (Spearman correlation = 0.60, $P<10^{-10}$, after removing 3 overlapping genes). To understand what drives this shared pattern, we investigated the role of gene constraint, i.e., the intolerance to mutational changes for genes frequently affected across neuropsychiatric disorders[1,2,35,44,45]. When we progressively removed the most constrained genes (measured by loss of function Z-score (LoF-Z)[46], which quantifies the deviation of observed likely gene disrupting (LGD) mutations from expected, in healthy populations) from the gene sets associated with both disorders, the correlation between ASD and SCZ rapidly decreased, reaching zero after removing ~25 of the genes, while removing the least constrained genes had no effect on the correlation (Fig. 2B). We then asked whether gene expression levels might also explain the shared correlation of mutation biases between ASD and SCZ, as both disorders involve genes highly expressed in the brain. Interestingly, in contrast to gene constraint, removing highly expressed genes had little impact on the cell type bias correlation (Suppl. Fig. 5). These findings suggest that highly constrained genes – those most resistant to (LGD) mutations in healthy populations – tend to be more specifically expressed in cell types that are mutationally biased in both disorders.

Several specific superclusters (hierarchically organized groups of brain cell type clusters sharing transcriptional signatures in the human brain cell atlas) are strongly biased by mutations in both ASD and SCZ, notably including excitatory neurons in the amygdala and hippocampus as well as Deep-layer intratelencephalic (IT) neurons (Fig. 2C, Suppl. Fig. 6A-D). These findings are consistent with several previous studies reporting frequent perturbations of these neurons in brain disorders. For example, amygdalar neurons and their cortical and hippocampal projections are implicated in a broad range of behavioral disturbances in both SCZ and ASD, including deficits in emotion, motivation, and social interactions[47,48]. Additionally, the hippocampus is known to play a key role in social and cognitive deficits in ASD[49], as well as in learning deficits and positive symptoms associated with SCZ[50,51]. Deep-layer IT neurons, which are central to sensory processing, decision-making, and learning, are also affected in both disorders[52]. Collectively, these shared neuronal disruptions may underlie overlapping dysfunction of brain circuits mediating disorders' phenotypes[53].

Distinct cell type biases between ASD and SCZ

To identify disorder-specific mutational biases at the supercluster level, we assessed the differential bias between ASD and SCZ, quantified by the average difference in mutation bias across cell type clusters within a supercluster. This measure describes how strongly each particular supercluster is preferentially affected in one disorder compared to the other, which may

underlie the unique physiological and behavioral phenotypes associated with each disorder. We observed that mutations in ASD and SCZ are preferentially biased toward several specific neuron types (Fig. 2C). Among them, medium spiny neurons (MSNs) showed stronger differential biases in ASD compared to SCZ (Fig. 2D). Nearly all MSN cell types exhibited stronger ASD mutation biases, with a few also exhibiting SCZ bias. This agrees with previous findings implicating MSNs in ASD[54] and multiple experimental studies[55,56]. In contrast, GABAergic interneurons, including MGE-, CGE-derived, and Lamp5-LHX6/Chandelier interneurons showed the strongest differential biases towards SCZ compared to ASD (Fig. 2 CEF). As mentioned above, while overall IQ may be similar between SCZ and ASD cohorts, cognitive impairment is thought to be widespread in schizophrenia while cognitive symptoms in high-functioning ASD are often more localized and specific. Considering this, we explored what neuron types are more affected in ASD probands with ID compared to ASD probands without ID. This analysis showed that, CGE interneurons were also showed stronger differential biases in ASD with ID (Fig. 2G, Suppl. Fig 6G), revealing the potential role of CGE cell types in cognitive dysfunctions observed in both ASD with ID and SCZ.

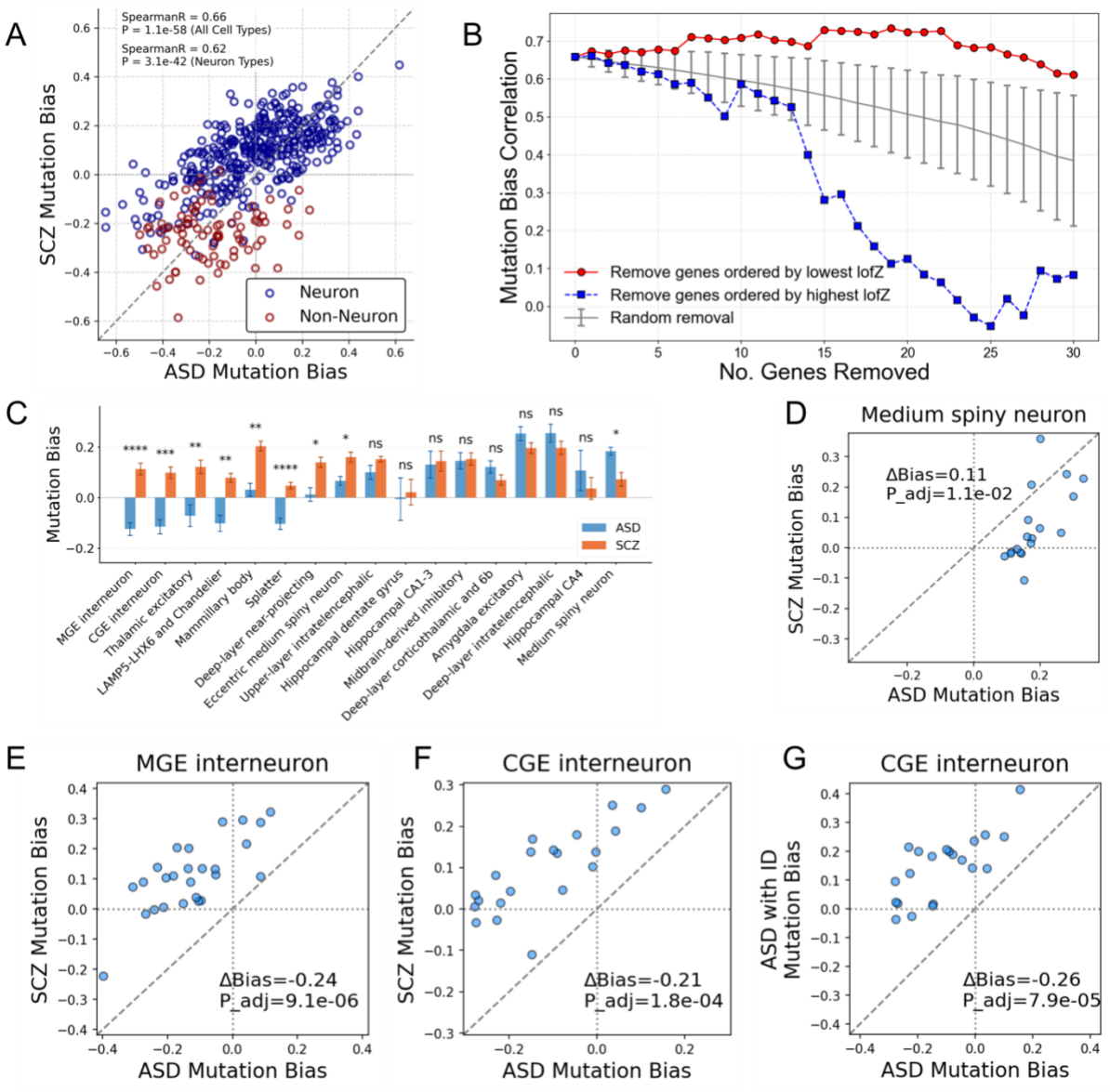

Figure 2. ASD and SCZ Mutation bias towards different brain cell types. A. Scatter plot showing correlation of mutation biases between ASD and SCZ across all cell types. Neuronal (blue) and non-neuronal (brown) cell types are indicated. Strong correlation is observed for both all cell types (Spearman R= 0.66) and neuron-specific analysis (Spearman R = 0.62). **B.** Spearman correlation of cell type bias between ASD and SCZ genes, assessed by sequential gene removal. The red line represents the bias correlation when removing genes with the lowest constraint (lofZ) scores, while the blue line represents the correlation when removing genes with the highest constraint scores. The gray line shows the average correlation for random gene removals, with error bars indicating ±1 standard deviation from the mean of random removals. **C.** Bar plot comparing mutation biases across superclusters between ASD (blue) and SCZ (orange). Superclusters showing positive mutation bias for at least one disorder are displayed in the figure and sorted by average differential bias between ASD and SCZ. Error bars represent standard error cross cluster biases from corresponding supercluster. Asterisks indicate significance level between groups (*: P < 0.05. **: P < 0.01. ***: P < 0.001, ****: P < 0.0001, ns=not significant). Detailed data can be found in Supplementary table 4. **D-G.** Detailed comparison of mutation biases in specific neuron superclusters, each point representing a cell type cluster from the corresponding supercluster, P-values were calculated based on Mann–Whitney U test with false discovery rate (FDR) correction. **(D)** Medium spiny neurons show stronger bias in ASD (adjusted P = 1.1e-02), **(E)** MGE interneurons exhibit stronger bias in SCZ (adjusted P = 9.1e-06), **(F)** CGE interneurons display bias toward SCZ (adjusted P = 1.8e-04),

and **(G)** CGE interneurons show stronger bias when comparing ASD with ID to ASD (adjusted P = 7.9e-05). Detailed data can be found in Supplementary table 2 and 3.

VIP+ interneurons are strongly affected in multiple psychiatric phenotypes with cognitive impairments.

To further explore the involvement of CGE interneurons in cognitive function, we analyzed additional cohorts with cognitive phenotypes (Fig. 3A). In the Developmental Disorders and Intellectual Disability (DD/ID) cohort[45], which is characterized by severe cognitive impairments, we also observed a strong bias towards CGE interneurons (Fig. 3A, grey, Suppl. Fig. 6F). Furthermore, analysis of the UK Biobank rare protein-coding variants associated with cognitive functions, including Verbal-Numerical Reasoning (VNR), Reaction Time (RT), and Educational Attainment (EDU))[57], revealed that genes negatively associated with VNR (mutations in these genes tend to lead to worse VNR performance) exhibited a pronounced bias toward CGE interneurons compared to genes positively associated with VNR (Suppl. Fig. 6E). The consistent strong CGE interneuron mutation bias across different cohorts suggests that these neurons play a key role in cognitive processes. In contrast, MGE and Lamp5-LHX6/Chandelier interneurons did not demonstrate comparably strong mutation biases across the cognitive phenotype cohorts we examined (Suppl. Fig. 7).

To quantify the relationship between expression biases toward different human brain cell types and cognitive function, we calculated a Phenotype Bias Sensitivity (PBS) score for each cell type using data for ASD probands with *de novo* mutations and corresponding full scale IQ (FSIQ) measured in the SPARK and ASC cohorts[2,58] (Suppl. Fig. 1). For a given cell type, PBS was calculated as the linear regression slope between the genes' expression bias toward that cell type and the average FSIQ of probands carrying *de novo* mutations in the gene (Suppl. Fig. 1B, Fig. 3C). In this way, more negative PBS values indicate that stronger gene expression biases towards a cell type are associated with lower probands' IQ. The statistical significance of PBS for cell clusters was determined by a permutation approach, where we randomly reassigned FSIQ across probands and computed PBS for each permuted set, to create a null distribution (see Methods). The PBS calculations showed that the three major groups of interneurons, including CGE-derived interneurons, LAMP5-LHX6/Chandelier cells, and MGE-derived interneurons, exhibited the strongest PBS values (Fig. 3B). Further analysis of CGE interneuron subtypes revealed that vasoactive intestinal peptide-expressing (VIP+) interneurons consistently demonstrated significantly stronger PBS values (Fig. 3D). This suggests that mutations affecting VIP+ interneurons may be particularly important in determining cognitive outcomes in ASD probands. CGE-derived VIP+ interneurons modulate neural circuits by reducing inhibition and enhancing excitatory activity[59,60]—an essential mechanism for cognitive functions such as perception, attention, learning, and memory[61]. They achieve this by suppressing Sst+, Cck+, and possibly Pvalb+ interneurons[62,63], thereby indirectly amplifying pyramidal neuron activity. Moreover, VIP+ interneurons interact with cholinergic, serotonergic, and dopaminergic systems[63–68] to maintain the excitation-inhibition balance critical for network stability and effective cognitive processing[61].

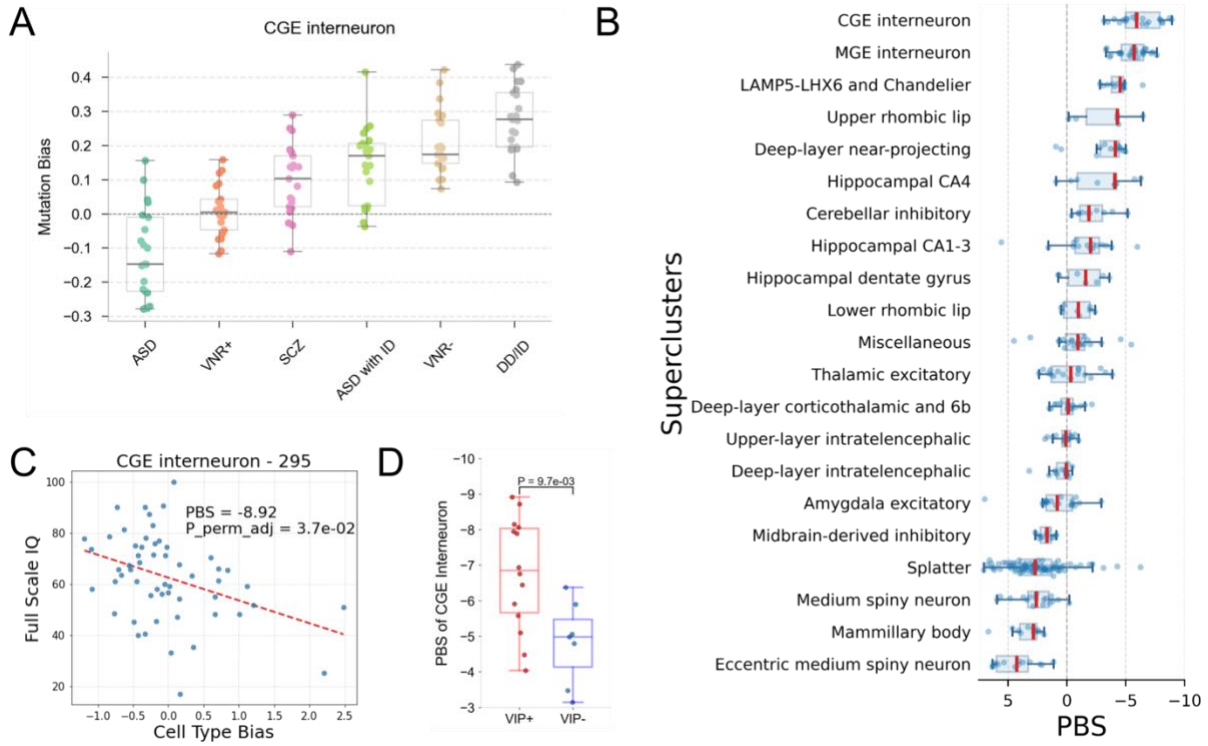

Figure 3. CGE interneurons are impacted in multiple cohorts with cognitive abnormalities. A. CGE interneuron mutation biases across different cohorts shows increasing bias in disorders with cognitive deficits. Each dot represents a CGE interneuron subtype. Comparison includes ASD (without ID) (adjusted P = 1), verbal-numerical reasoning (VNR-: adjusted P = 3.3e-09, VNR+: adjusted P = 1), schizophrenia (SCZ) (adjusted P = 0.19), ASD with ID (adjusted P = 7.4e-03), and developmental disorders/intellectual disability (DD/ID) (adjusted P = 7.5e-08). P values were calculated with Mann-Whitney U test with FDR correction. **B.** Phenotype Bias Sensitivity (PBS) analysis across neuronal cell types reveals strongest correlation with Full Scale IQ (FSIQ). Negative PBS values indicate genes with stronger cell type bias are associated with lower FSIQ scores. CGE interneuron average PBS=-6.78, adjusted P=0.014, LAMP5-LHX6 and Chandelier, average PBS=-6.65, adjusted P=0.03. P values were calculated with mutation permutation test with FDR correction. Detailed data can be found in supplementary table 5. **C.** Association between cell type bias and FSIQ for CGE interneuron cluster 295 (VIP+), which is the cell type has strongest PBS. Each dot represents a High confident ASD gene, with FSIQ averaged across multiple probands with mutation from the gene shown on the y-axis. The x-axis displays each gene's bias towards cell type 295. **D.** Comparison of PBS values between VIP+ and VIP- CGE interneuron subtypes shows stronger association with cognitive phenotypes in VIP+ interneurons (PBS difference = -1.96, P = 9.7e-03, Mann-Whitney U test).

VIP+ interneurons are strongly affected by 22q11.2 deletions

Copy number variants (CNVs) consistently stand out as highly penetrant genetic risks for SCZ and ASD[11,32,69,70]. The 22q11.2 deletion syndrome is a neurodevelopmental disorder marked by a significantly elevated risk of schizophrenia in adulthood, along with comorbidities such as ASD and intellectual disability[10,71]. Cognitive impairment is a key feature of 22q11.2 deletion syndrome, with nearly half of affected individuals displaying an IQ below 70[72,73]. Consistent with most disease-predisposing CNVs, the full range of phenotypic outcomes and disease symptoms results from the synergistic effects of multiple genes within the 22q11.2 deletion[10]. Given the significant SCZ risk and cognitive disability phenotypes associated with the 22q11.2 deletion we investigated

next the bias toward CGE and other interneurons for genes in the deletions. The 22q11.2 deletions occur in two primary forms: a 3 Mb deletion (46 genes) and a smaller 1.5 Mb deletion (28 genes). Analysis of cell type biases for genes in the 3 Mb deletion (Suppl. Fig. 8) revealed a substantial impact toward CGE-derived interneurons compared to other major interneuron types (Fig. 4A), suggesting a crucial link to cognitive function and IQ. Notably, among CGE interneuron cell type clusters, VIP+ interneurons exhibited significantly stronger biases compared to biased toward VIP- CGE cell types (Fig. 4B). This pattern remains consistent when examining genes within the 1.5 Mb deletion. This selective impact on VIP+ interneurons over other CGE interneuron types suggests that 22q11.2 deletion may exert a particularly pronounced impact on the VIP+ interneurons, potentially contributing to the severe cognitive and behavioral phenotypes associated with 22q11.2 deletion syndrome.

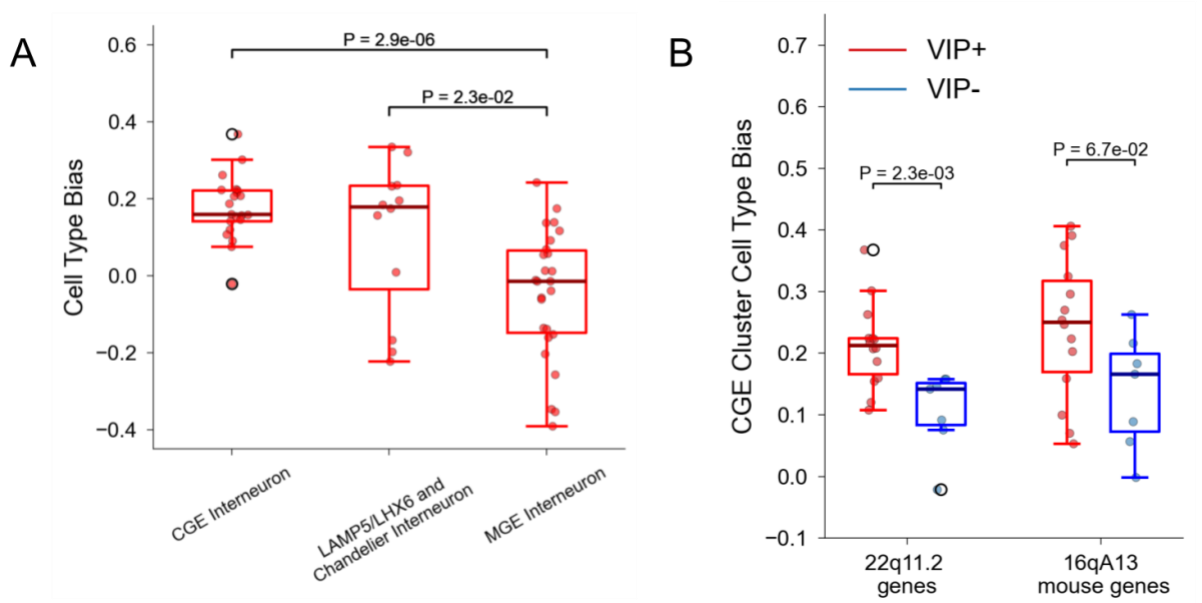

Figure 4. VIP+ CGE interneurons are preferentially affected by 22q.11.2 deletion genes. (A) Boxplot showing expression biases for three major interneuron types (CGE interneurons, Lamp5/LHX6 and Chandelier cells, and MGE interneurons) in the 22q11.2 deletion region. CGE interneurons exhibit the strongest bias compared to other interneuron populations (P-values shown for pairwise comparisons, Mann-Whitney U-test). Complete data can be found in Supplementary table 2**. (B)** The CGE interneuron cell type bias crosses different gene sets. including complete 22q.11.2 genes, genes included in 1.5MB deletion which equivalent to mouse 16qA13 deletion. VIP+ CGE types shown in red and VIP- CGE types shown in blue. Difference between VIP+ and VIP- bias is significant for all 22q.11.2 genes and suggestive for 1.5MB deletion genes (P=2.3e-03 and 6.7e-02, respectively, Mann-Whitney U-test.)

Altered VIP+ interneuron activity and population specificity in a mouse model for the 22q11.2 deletion syndrome

Having identified a robust genetic association between mutation biases toward CGE and VIP+ cell types and cognitive phenotypes across multiple genetic disorders, including the 22q11.2 deletion syndrome, we next experimentally investigated whether and how this bias is reflected in altered function and integration of these interneurons within hippocampal microcircuits. To this end we used the *Df(16)A*$^{+/-}$ mouse model, which faithfully recapitulates the human 1.5 Mb 22q11.2 deletion[9,29,31,74]. This model, known for deficits in working and episodic memory, synaptic

plasticity, and cortical and hippocampal development, has proven invaluable for uncovering novel biological pathways relevant to cognitive disfunction and psychiatric disorders[10,31,32,71,74–77]. By complementing our computational analyses with in vivo assessments, we examined the physiological impact of the 22q11.2 deletion on specific CGE/VIP+ subtypes—beyond the resolution of our computational methods—thus advancing our understanding of the cellular mechanisms by which CGE-derived interneurons mediate cognitive processes are disrupted in the 22q11.2 deletion syndrome.

To examine VIP+ interneuron activity *in vivo* we crossed *Df(16)A*$^{+/-}$ mice with VIP-Cre mice and locally injected an adenovirus carrying a floxed GCaMP8m or GCaMP7f calcium indicator into CA1 to selectively express GCaMP in VIP+ interneurons (Suppl. Fig. 9A). Using two-photon three-dimensional acousto-optic deflector (3D-AOD)[78–80] microscopy, we then recorded VIP+ interneuron activity in a 3D volume within the dorsal hippocampal CA1 region (Suppl. Fig. 9B/C/D). *Post hoc* immunohistochemistry[28,78,81] (see Methods) allowed us to identify four major VIP+ interneuron subtypes: interneuron-selective interneurons type 2 (ISI2), interneuron-selective interneurons type 3 (ISI3), VIP+ cholecystokinin basket cells (CCKBCs), and a group of VIP-expressing cells, referred to as "VIP+ only" (VIPo) cells, that were immunonegative for all other tested markers[59,82,83]. The distribution of these subtypes across hippocampal layers did not significantly differ between wild type and *Df(16)A*$^{+/-}$ mice (Suppl. Fig. 9G/H), and comparable numbers of each interneuron subtype were recorded from both wild type and mutant genotype (Suppl. Fig. 9I). Thus our analysis did not find any evidence suggesting the 22q11.2 deletion affects the number or proportion of VIP+ interneuron subtypes in the hippocampal CA1 region.

As was established previously, global interneuron activity is strongly driven by ambulatory state[84–87] and in treadmill-based experiments we reliably observed that locomotion is the greatest predictor of global interneuron activity[28,78,88]. To investigate locomotion-related activity of hippocampal VIP+ interneurons, mice were next trained to run on a head-fixed, cue-rich 2-meter treadmill for randomly distributed water rewards while undergoing calcium imaging (Fig. 5A)[28,78,81]. Behavioral metrics, including laps run, licking, and region occupancy in the belt during the 10-minute trials, were similar across genotypes (Suppl. Fig. 9J-M). Expected locomotion-related activity patterns were preserved across genotypes, with ISI3, ISI2, and VIPo subtypes positively correlated with movement, and VIP+ CCKBCs anticorrelated (Fig. 5B)[78,89]. However, ISI3 and ISI2 cell activity exhibited a significantly reduced correlation with locomotion (Fig. 5C), and ISI3, ISI2, and VIPo interneurons showed visibly reduced calcium transient amplitudes in *Df(16)A*$^{+/-}$ mice (Fig. 5B). Due to the spike-like activity of ISI3, ISI2, and VIPo cells we were able to perform transient waveform analysis (see Methods[90]). This analysis confirmed reduced amplitudes in ISI3, ISI2, and VIPo cells (Fig. 5D-J), while VIPo cell transients uniquely occurred at a higher frequency (Fig. 5J). Reward responses, accessed by Peri-event Time Averages (PETA, see Methods), exhibited genotype-dependent differences, including reduced VIPo response amplitudes and enhanced ISI2 and ISI3 response amplitudes (Fig. 5K,L), suggesting that ISIs in mutant mice exhibit heightened sensitivity to random salient features[88]. Overall, these results show that VIP+ interneurons in the hippocampal CA1 region exhibit reduced *in vivo* activity dynamics in the 22q11.2 deletion model and that reward responses are significantly altered among specific VIP+ subtypes, demonstrating physiological consequences of the genetic perturbation inferred by our computational analysis.

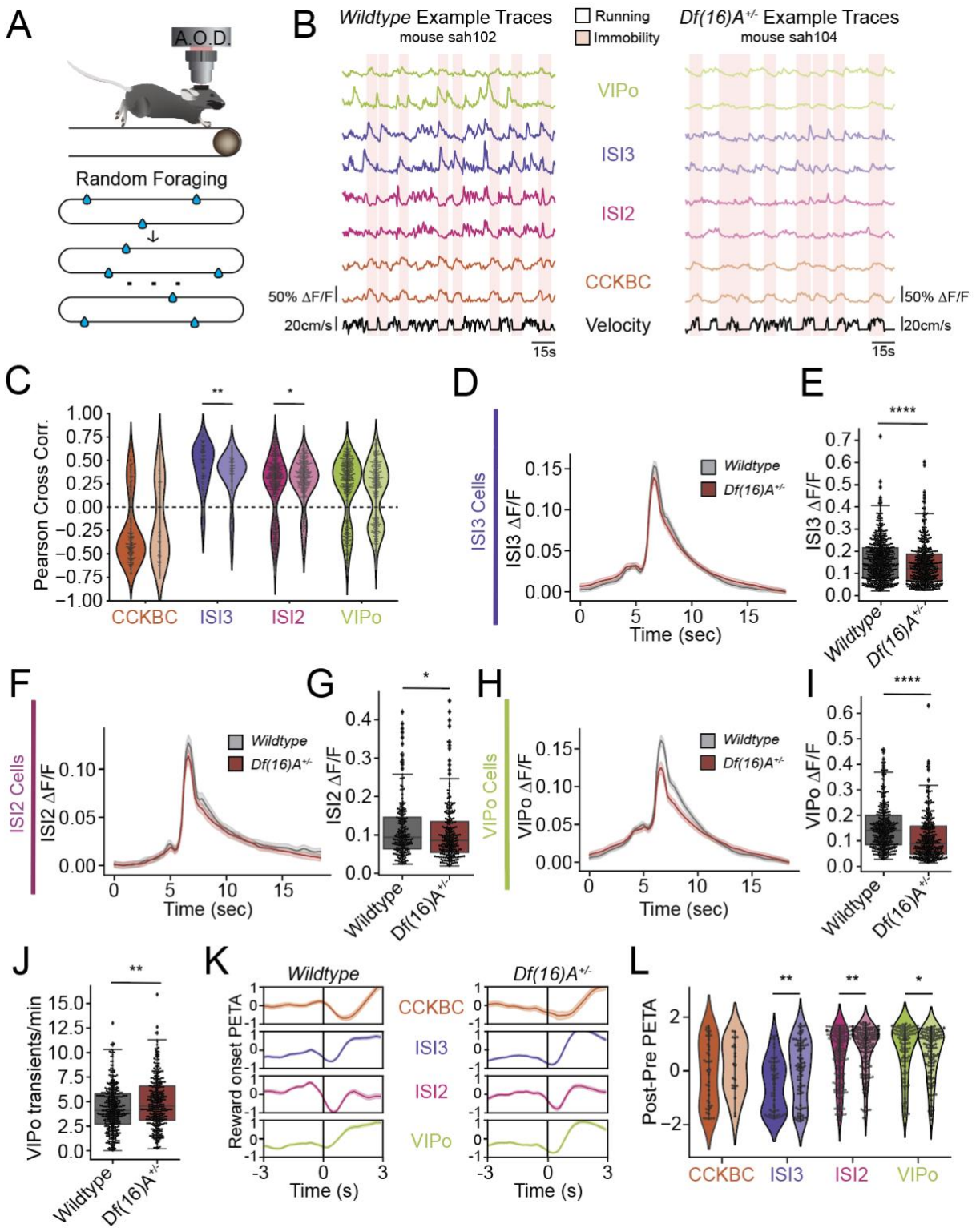

Figure 5: Baseline changes in VIP+ cell type calcium dynamics in mutant mice. A. Imaging and behavior schematic: mice are trained to run on a cue-rich belt to expect random water rewards to be deposited across the belt (bottom) while head-fixed and imaged with 2-photon 3D-AOD microscopy (top). **B.** Example traces from all four VIP+ cell types detected in a single session from a Wildtype littermate (left) and a *Df(16)A*$^{+/-}$ (right) mouse. **C.** Pearson correlation coefficients of mouse velocity against average subtype calcium activity. **D.** Waveform comparison of average

detected calcium transient from wildtype littermates (black) and *Df(16)A*$^{+/-}$ (brown) ISI3 cells. **E.** Average amplitude of detected ISI3 waveforms compared between genotypes. **F.** Waveform comparison of average detected calcium transients from wildtype littermates (black) and Df(16)A$^{+/-}$ (brown) ISI2 cells. **G.** Average amplitude of detected ISI2 waveforms compared between genotypes. **H.** Waveform comparison of average detected calcium transients from wildtype littermates (black) and *Df(16)A*$^{+/-}$ (brown) VIPo cells. **I.** Average amplitude of detected VIPo waveforms compared between genotypes. **J.** Number of transients from VIPo cells per cell between genotypes. **K.** Averaged z-scored reward-onset peri-event time averages (PETAs) between -1.0 and 1.0 z-scores by cell type across all cells within cell type during the Random Foraging task for 3 seconds pre- and 3 seconds post-event. **L.** Post - Pre PETA responses per cell type before and after reward onset comparing the 3 seconds pre- to 3 seconds post-event. *CCKBC:* VIP+ and cholecystokinin + basket cell; *ISI3:* Interneuron-selective interneuron type 3; *ISI2:* Interneuron-selective interneuron type 2; *VIPo*: VIP+/Cal-/M2R-/CCK- cells in layer oriens or layer pyramidale. *: $P < 0.05$. **: $P < 0.01$. ****: $P < 0.0001$. See Suppl. Table 1 for detailed statistics.

Hippocampal place cells, a subset of pyramidal neurons, are active in specific environmental locations and provide cellular substrates for episodic memory and goal-directed spatial learning[91,92]. In *Df(16)A*$^{+/-}$ mice, our previous study revealed significant impairments in learning performance when both contextual cues and reward locations were altered during a spatial navigation task[76]. These learning deficits were associated with reduced long-term stability of place fields, impaired context-related remapping and plasticity, and a lack of reward-related reorganization. Further investigation showed that parvalbumin- and somatostatin-expressing GABAergic interneurons, which are directly inhibited by VIP+ cell activity, displayed diminished place fields and heightened reward-related activity, likely contributing to the observed place cell deficits[28]. Changes in activity dynamics of VIP+ cells in dorsal CA1 may also reflect altered spatial information encoding by these cells. To explore this, we next evaluated how well mouse position could be decoded based on VIP+ subtype activity during random foraging (Fig. 5A) by training a support vector machine using all recorded IN activity (Fig. 6A). Decoding error did not differ between genotypes when the total number of imaged cells per session was not normalized. However, when controlling for the number of cells tested (Fig. 6B) or the number of laps run per session (Fig. 6C), decoding error was significantly higher in *Df(16)A*$^{+/-}$ mice, indicating that individual mutant cells carry less spatial information. Furthermore, analysis of place preference in VIP+ cell activity revealed that fewer VIP+ cells in *Df(16)A*$^{+/-}$ mice exhibited significant place fields, with a reduced proportion displaying at least one place field (Fig. 6D). These findings demonstrate that VIP+ interneurons in the 22q11.2 deletion model exhibit markedly impaired spatial encoding within the CA1 microcircuit.

Local brain circuits balance coordinated and unique activity depending on input properties, connectivity, and brain state. Taking advantage of our simultaneous recordings across multiple VIP+ subtypes in our experiments, we computed pairwise Pearson's correlation coefficients between calcium activity traces within and between different VIP+ interneuron subtypes (see Methods) and found that VIP+ cells in *Df(16)A*$^{+/-}$ mice displayed unusually high correlations during random foraging between subtypes. This suggests a loss of subtype-specific heterogeneity of *in vivo* activity dynamics, particularly among disinhibitory VIP+ subtypes, indicating a potential microcircuit-level disruption and impaired fine-scale coordination between VIP+ interneuron subtypes (Fig. 6E/F). These findings reveal that VIP+ interneurons in the CA1 region of *Df(16)A*$^{+/-}$ mice exhibit impaired spatial encoding — reflected in increased decoding errors and reduced place preference — and that this disruption is also accompanied by a loss of subtype-specific

heterogeneity, as indicated by unusually high inter-subtype correlations during foraging. These physiological consequences align with our computational analyses and illuminate how perturbations in specific subtypes of VIP+ interneurons can disrupt network dynamics and information processing important for cognition.

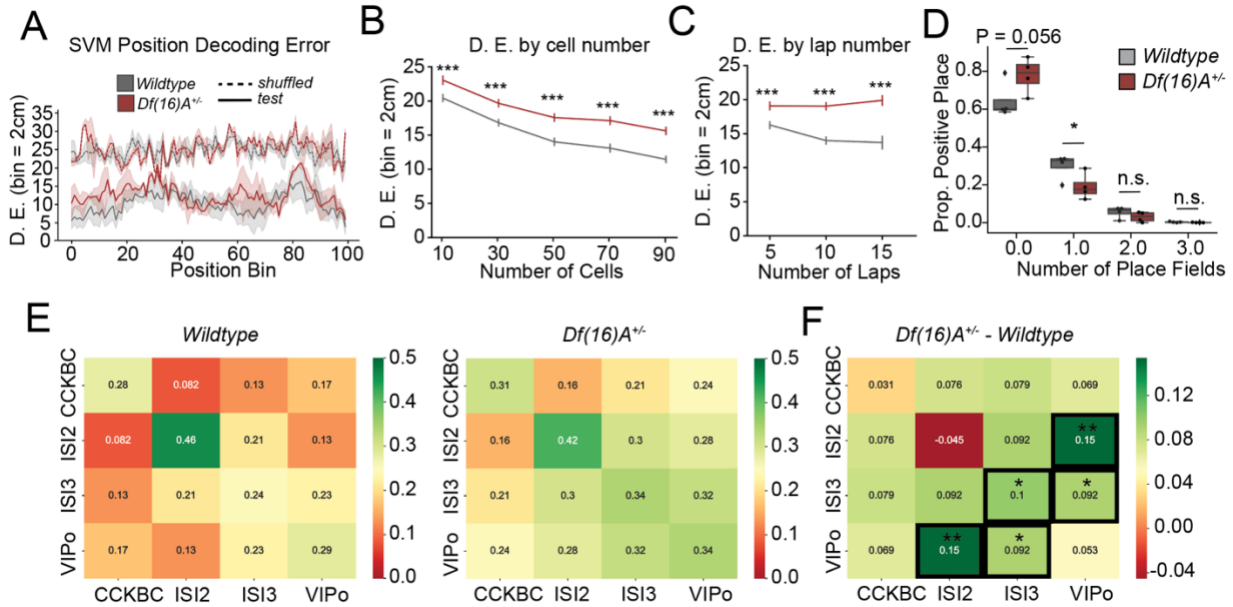

Figure 6. Reduced specificity in *Df(16)A*$^{+/-}$ VIP+ interneuron population activity. A. All recorded VIP+ interneuron activity was used to train a support vector machine (*SVM*) to decode discrete position bins (*D.E.*: decoding error) across the belt. Each bin is equivalent to 2 cm. **B.** SVM results bootstrapped 100 times by number of cells used per genotype per bin. **C.** SVM results bootstrapped 100 times by the number of laps used per genotype per bin. **D.** Proportion of positive place fields detected using the Peak Place method. **E.** Pairwise Pearson's correlation coefficient value matrix between cell types of ($\Delta F/F$) traces across the trial during the Random Foraging paradigm from WT (left) and *Df(16)A*$^{+/-}$ (right). **F.** Comparative differences between cell type correlated activity between genotypes. *CCKBC:* VIP+ and cholecystokinin + basket cell; *ISI3:* Interneuron-selective interneuron type 3; *ISI2:* Interneuron-selective interneuron type 2; *VIPo*: VIP+/Cal-/M2R-/CCK- cells in layer oriens or layer pyramidale. *: P < 0.05. **: P < 0.01. ***: P < 0.001. See Suppl. Table 1 for detailed statistics.

Discussion

Cognitive dysfunction is central to psychopathology, as many psychiatric conditions share overlapping yet challenging-to-treat cognitive impairments[15–18,36,72]. For instance, schizophrenia often presents with deficits in executive functioning and working memory[7,8]. Similarly, ASD cases driven by rare damaging mutations[54,93] are often associated with pronounced cognitive deficits. Cognitive disabilities are also common in such genetic conditions as 22q11.2 deletion syndrome, where affected individuals frequently display difficulties with attention, working memory, and executive processes[10,71,72]. In this study we focused on understanding neuronal mutation biases of rare highly penetrant genetic variants. We observed a strong correlation between cell type biases in ASD and SCZ that was primarily driven by mutations in highly constrained genes. We also identified several cell type biases that were more pronounced in each disorder, possibly contributing to disorder-specific symptoms. For example, medium spiny neurons of the striatum showed a significantly stronger mutation bias in ASD compared to SCZ, consistent with ASD's core symptoms of repetitive behaviors and social impairments, which are frequently associated with striatal dysfunction[55,56]. In contrast, multiple types of interneurons exhibited stronger mutation bias in SCZ, consistent with recent GWAS-based studies[21,22], particularly parvalbumin-expressing interneurons crucial for gamma oscillations and cognitive processing[94,95], as well as somatostatin-expressing interneurons important for information processing[96]. Supporting these findings, transcriptomic studies have identified alterations in these interneuron populations in SCZ patients[97].

Our genetic analysis revealed dysfunction in CGE-derived GABAergic interneurons as a central vulnerability contributing to cognitive deficits across multiple psychiatric conditions (Fig. 3). Specifically, we found that CGE interneurons are more affected in SCZ compared to high-functioning ASD, consistent with the cognitive impairments being a core and defining symptom of SCZ[16,17]. We also observed strong genetic impact on CGE interneurons in low-functioning versus high-functioning ASD, in intellectual disability and in 22q11.2 deletion syndrome. Verbal and numerical reasoning phenotypes available in the UK Biobank[57], which generally reflect milder cognitive impairments compared to psychiatric disorders, showed significant association with mutational impact on CGE interneurons and on spiny neurons of the striatum, with the latter previously implicated in studies of human intelligence[98]. Of note, impaired disinhibition and CGE-derived VIP+ interneuron dysfunction have been previously described in other neurodevelopmental disorders[99–101]. In Rett syndrome, for example, selective deletion of Mecp2 in VIP+ interneurons, but not in Pvalb+ or Sst+ interneurons, leads to deficits in cortical state transitions and social memory[100]. In Dravet syndrome, SCN1A mutations lead to persistent VIP+ interneuron dysfunction in juvenile and adult mutant mice, contributing to social and cognitive deficits[99,101].

Because VIP+ interneurons inhibit other major interneuron subtypes, their activation increases pyramidal neuron excitability, thereby improving the detection of low-contrast signals[83,102]. In this way, these interneurons are essential for learning and attention, as they respond to salient stimuli by adjusting overall neural excitability. For instance, during fear conditioning, blocking VIP+ interneurons disrupts projection neuron activity and impairs fear learning[60]. In the hippocampal

CA1 region, proper VIP+ interneuron function is vital for spatial learning because excessive inhibition of pyramidal neurons hinders place cell remapping and performance, while their activation enhances learning outcomes[88]. Similarly, in the prefrontal cortex, activation of VIP+ interneurons improves working memory and attention, whereas activation of Pvalb+, Sst+, or pyramidal neurons produced detrimental effects[68,88,102,103].

Following our computational genetics analysis implicating a strong CGE/VIP+ interneuron mutation bias in cognitive disorders, including 22q11.2 deletion syndrome, we evaluated VIP+ interneuron activity *in vivo* using the *Df(16)A*$^{+/-}$ mouse model. To that end, using advanced two-photon (2P) calcium imaging in the well-characterized hippocampal CA1 microcircuit we measured VIP+ interneuron activity during a spatial navigation task. We observed significant defects at both the cellular and circuit levels, likely contributing to broader hippocampal dysfunction previously reported in this mouse model[28,76]. Specifically, VIP+ interneurons exhibited dampened calcium activity, suggesting a reduction in the top-down disinhibition[61,104] normally exerted by these cells in cortical circuits. In addition, we found a reduction in the spatial information carried by their activity. Because synaptic plasticity is critical for fine-tuning synaptic connections and forming dynamic spatial representations and episodic memories, this reduction likely reflects impaired plasticity mechanisms. Such impairment may hinder MGE-derived interneurons and pyramidal neurons from effectively encoding and updating spatial information[28,76], ultimately disrupting the integration of spatial signals within the hippocampal network. Furthermore, VIP+ interneuron subtypes exhibited increased correlation in their *in vivo* activity, particularly among interneuron-selective interneuron subtypes. This suggests a loss of their normally distinct activity patterns, leading to reduced informational diversity in the circuit. Impaired disinhibition within the CA1 microcircuit in patients with 22q11.2 deletion syndrome disrupt the processing and integration of salient inputs, resulting in cognitive deficits associated with hippocampal dysfunction. Given that VIP+ disinhibitory motifs are highly conserved across cortical circuits[59,60,105], the deficits we uncovered in the CA1 circuit are likely pervasive across neocortical brain regions.

While further research is needed to link specific disease-related behaviors to VIP+ interneuron circuit dysfunction, our combined computational and experimental results suggest that disruption in VIP+ interneuron activity may be a key driver of cognitive deficits in 22q11.2 deletion syndrome and in other neurodevelopmental and psychiatric disorders[106]. These findings position CGE/VIP+ interneurons as a critical and targetable point of dysfunction. Given the persistent cognitive comorbidities across multiple psychiatric disorders, pharmacologically targeting VIP+ interneuron dysfunction, especially during the chronic phase, may offer a viable treatment strategy. This emphasizes the need for cell-type-specific tools to address VIP+ interneuron dysfunction across a range of brain disorders.

METHODS

Genetic analysis:

Rare mutation genetic data for neuropsychiatric disorders and phenotypes

For the analysis on cell type mutation biases of ASD and SCZ, we primarily used the aggregated mutation data obtained from the SFARI Simons Foundation Powering Autism Research for Knowledge (SPARK) cohort, and The Schizophrenia Exome Sequencing Meta-Analysis (SCHEMA). In the SPARK study[2], de novo mutations were identified through familial sequencing of 42,607 ASD probands and 8,267 unaffected siblings. We focused our analysis on de novo likely gene disrupting (LGD) mutations and damaging missense (Dmis) mutations. Dmis mutations were identified based on the REVEL score[107], which estimates the probability of a missense mutation to be pathogenic; mutations with REVEL scores higher than 0.5 were defined as deleterious. For our main analysis, we used 61 genes that reached exome-wide significance (P-value < 1.3×10^{-6}) identified in the SPARK study, using the DeNovoWEST statistical model[45].

In the SCHEMA study[1], which analyzed 24,248 schizophrenia cases and 97,322 controls, we selected the top 61 genes with strongest association for our primary analysis (p-value < 1.0×10^{-3} or FDR<0.3). Dmis mutations were identified based on the MPC score[108]. two tiers established: MPC score > 3 (mis3) and 3 > MPC > 2 (mis2). We included LGD and mis3 mutations in our main analysis since they are most damaging mutation type.

To analyze cell type biases across different cohorts with cognitive abnormalities, we examined several additional gene sets beyond ASD and SCZ. We included genes within the 22q11.2 deletion region as defined by Karayiorgou et al[10]. We also analyzed genes associated with adult cognitive function from the UK Biobank study by Chen et al[57], which identified rare coding mutations linked to educational attainment (EDU), reaction time (RT), and verbal-numerical reasoning (VNR). For each cognitive phenotype, we selected the top 61 genes based on statistical significance (smallest p-values). We separately analyzed genes with positive and negative impacts (indicated by the beta coefficients of gene-phenotype associations), focusing on European population data for optimal statistical power.

Additionally, we included genes associated with developmental disorders and intellectual disability (DD/ID) from Kaplanis et al[45], selecting the top 61 genes according to DeNovoWEST p-values. To ensure comparable bias magnitudes across analyses, we consistently used 61 genes for each cohort to match the number of genome-wide significant genes identified in the SPARK ASD study, except for 22q11.2 genes, since the deletion region consists of only 46 genes.

Human whole brain single cell data

For our analysis, we used a recent human brain single-nucleus sequencing dataset from the Allen Institute[33], comprising 3,369,219 nuclei sampled from 105 regions across the entire brain of three donors. To the best of our knowledge, this dataset represents the first comprehensive human brain single-cell atlas with extensive regional coverage. This comprehensive sampling is crucial for accurately identifying affected brain cell types without regional sampling biases. The dataset

contains 461 clusters and 3,313 subclusters organized into 31 superclusters, reflecting their transcriptional similarities and developmental origins.

Cell type mutation bias

We calculated cell type mutation biases at the cluster level (which we refer as cell type throughout the text) for each disorder or phenotype. First, for each cell type cluster, we computed gene expression levels by averaging $\log_2 \mathrm{UMI} + 1$ values across all individual cells assigned to that cluster. $\log_2$transformation was applied to make expression values more robust to outliers and extreme values. For each disorder-associated gene, we then characterized its expression specificity toward each cell type cluster. We calculated expression specificity Z-scores for each gene in a given cell type by comparing its expression level in that cell type to its expression across all 461 cell types in the atlas, as shown in equation 1.

$$Z_{g,ct} = \frac{E_{g,ct} - <E_g>}{\sigma_g} \qquad (1)$$

where $E_{g,ct}$ is the expression of a gene g in a cell type ct, $< E_g >$ is the average expression level of the gene g across all cell types, and σ_g is the standard deviation of the gene g expression across all cell types.

The high granularity at the cell cluster level combined with the inherent sparsity of single-cell sequencing data meant that some cell types had too few cells for reliable estimation of expression levels. To mitigate noise in our cell type bias calculations, we capped the cell type specificity scores at a maximum of 5 and a minimum of -5, preventing individual genes from having unreasonably high specificity values that could dominate the mutational bias profile of a disease cohort. For genes with zero expression in certain cell types, we consistently assigned the minimum specificity score, ensuring uniform handling of non-expressed genes across all cell types.

To account for variability in expression specificity that may arise simply due to different gene expression levels across cell types (reflected in total UMI counts), we used a Z′-score, to characterize how a gene's specificity Z-score (Equation 1) in a given cell type deviates from the distribution of Z-scores of random genes with similar overall brain expression levels. To identify genes with similar expression levels, we first ranked all genes based on their overall brain expression (defined as the sum of expression levels across all individual cells in the human brain cell atlas). We then uniformly sampled 1,000 genes within ±5% of the target gene's expression level. Our validation tests confirmed that results were not sensitive to the sampling interval range or the sampling kernel function. This comparison to genes with similar expression levels ensures that neither the expression level of target genes nor cell types skews or artificially influences the specificity measurement. Thus, for each disorder gene and each brain cell type we computed the Z′-score:

$$Z'_{g,ct} = \frac{Z_{g,ct} - <Z_{ct}>_M}{\sigma_{M,ct}} \qquad (2)$$

where the label M corresponds to a set of sampled genes with expression levels similar to the gene g, $< Z_{ct} >_M$ represents the average Z-score of genes in the set M for the cell type ct, and $\sigma_{M,ct}$ represents the standard deviation of Z-scores of genes in the set M for the cell type ct.

Finally, to calculate cell type-specific mutation biases across each disorder cohort, we integrated gene expression specificities (Z′-score, Equation 2) with their corresponding genetic burden. This weighting approach allows us to account for the relative genetic contribution of individual genes to the disorder. For the ASD cohort, we quantified each gene's contribution using a weighting formula where the mutation weight for gene g was determined as follows:

$$w_g = n_{g,LGD} + n_{g,Dmis} \quad (3)$$

where $n_{g,LGD}$ and $n_{g,Dmis}$ are the numbers of observed *de novo* LGD and Dmis mutations in gene g.

For the SCZ cohort, we calculated mutation biases by integrating both de novo and inherited mutations identified in case-control studies. Since the genetic evidence comes from these two distinct sources, we computed "effective mutation counts" to standardize their contributions. For case-control mutations, the effective count represents the excess mutations in cases after subtracting the expected counts (calculated by scaling control mutations by the case-control ratio). We applied this approach separately for each mutation class (LGD and Mis3) and then combined these values with observed de novo mutations, as shown in Equation 4:

$$n^{eff}_{g,mutType} = n^{case}_{g,mutType} - \frac{n^{ctrl}_{g,LGD}}{N_{ctrl}} \times N_{case} + n^{de\ novo}_{g,mutType}$$

$$w_g = n^{eff}_{g,LGD} + n^{eff}_{g,Mis3} \quad (4)$$

For genes associated with UK Biobank cognition phenotypes, we utilized each gene's effect size (beta coefficient from gene-phenotype association tests) as the gene weight. This approach assumes that genes with larger phenotypic effects contribute more significantly to cell type biases relevant to cognitive function. Unlike our approach with case-control studies, mutation counts were not employed for these analyses since VNR, EDU, and RT are quantitative traits analyzed through linear regression rather than categorical case-control comparisons.

$$w^{pheno}_g = beta^{pheno}_g \quad (5)$$

For genes in 22q.11 deletion, we applied a uniform weight for all genes ($w_g = 1$), as there is no systematic method available to determine the contribution of biases from each individual gene.

Based on the calculated mutation weight for each gene (Equations 3-5), the mutation bias for all disorder gene sets towards a cell type ct was then calculated as:

$$Mutation_Bias_{ct} = \frac{\sum_{g \in G} w_g \cdot Z'_{g,ct}}{\sum_{g \in G} w_g} \quad (6)$$

where the summation is over genes g in the set G containing all implicated genes of a disorder/phenotype, and w_g is the mutation weight for each gene g. In summary, our cell type mutation bias approach identifies neuronal populations most strongly implicated in psychiatric disorders by integrating three key factors: genetic evidence (mutation frequency or association coefficients), cell type-specific expression patterns, and their statistical relationships with clinical phenotypes. This comprehensive measurement reveals which brain cell types are preferentially affected by high-confidence risk genes, providing insight into the neurobiological substrates of different psychiatric conditions.

Supercluster-level bias significance assessment

To determine the statistical significance of mutation biases for each disorder-supercluster combination, we employed the Mann-Whitney U test. This non-parametric approach compared the distribution of mutation biases across all cell type clusters within a given supercluster against the distribution of mutation biases in all clusters not belonging to that supercluster. This allowed us to identify superclusters with significantly elevated mutation biases relative to the background. Multiple comparison correction was performed using the Benjamini-Hochberg procedure to control the false discovery rate (FDR) across all tested superclusters, ensuring robust statistical inference.

Supercluster differential bias for a pair of disorders.

To identify disorder-specific mutational biases at the supercluster level, we assessed the differential bias between disorders (e.g., ASD vs. SCZ), quantified by the difference in mutation bias across cell type clusters within a supercluster. This differential bias measure describes how strongly each particular supercluster is preferentially affected in one disorder compared to another, potentially underlying the unique physiological and behavioral phenotypes associated with each condition.

$$\Delta Bias_s^{Pheno_{AB}} = \frac{\sum_{ct_1}^{ct_n} (Bias_{ct}^{Pheno_A} - Bias_{ct}^{Pheno_B})}{n} \quad (7)$$

Where $\Delta Bias_s^{Pheno_{AB}}{}_s$ is differential bias of Supercluster s between phenotype A and B. $Bias_{ct}^{Pheno_A}$ is mutation bias for cell type (cluster) for phenotype A. ct are n clusters from corresponding supercluster s.

To test whether these differential biases were statistically significant, we applied the Mann-Whitney U test to compare bias distributions between disorders for each superclass (e.g., CGE interneurons, MGE interneurons, medium spiny neurons). Multiple testing correction was implemented using the Benjamini-Hochberg procedure to control the false discovery rate across 31 superclusters. This approach allowed us to identify neuronal populations consistently showing disorder-specific vulnerability patterns across their constituent subtypes.

Phenotype bias sensitivity

Proband phenotypic data (Full Scale IQ) were obtained from ASC/SSC and from SPARK Phenotype Collection V6[58,109]. To investigate quantitative relationships between cell type biases and cognitive phenotypes, we performed linear regression analyses comparing Full Scale IQ (FSIQ) scores with cell type-specific expression biases using SPARK probands with FSIQ measurement (Supp Fig 1). Genes with exome wide significance were included in PBS analysis. For each gene harboring de novo mutations, we calculated the mean FSIQ across all affected probands. We then performed linear regression modeling these gene-level mean FSIQ scores as a function of cell type-specific gene expression biases.

For a given cell type ct the FSIQ of a proband can be represent as a linear function of cell type bias $Bias_{ct}$. The coefficient PBS_{ct} represent how sensitive the bias towards the cell type can determine the IQ.

$$FSIQ_g = a_{ct} + PBS_{ct} \times Bias_{ct,g} + e_{ct} \qquad (8)$$

Where $FSIQ_g$ is the average FSIQ for gene g (averaged across probands with de novo mutations in gene g). a_{ct} is intercept which approximately the average IQ of probands with De novo mutation in highly penetrate genes. $Bias_{ct,g}$ is expression bias of gene g towards cell type ct, PBS_{ct}, is the Phenotype Bias Sensitivity coefficient (regression slope), quantifying the relationship between cell type bias and IQ. e_{ct} represents residual variance in IQ not explained by cell type biases. The residual variance could be contributed by phenotypical heterogeneity within genes[110], common genetic variants[98], environmental factors and limitations in our cell type expression bias metrics. To assess statistical significance of PBS values, we compared observed values to a null distribution generated through permutation testing. In each permutation, we randomly reassigned FSIQ scores across probands included in the analysis, recalculated gene-level average IQs using these permuted values, and computed PBS for each cell type using Equation 7. For supercluster-level analysis, we used the mean PBS across all cell type clusters within a supercluster as the test statistic and compared it to the corresponding null distribution from the same permutation procedure.

Mouse Experiments:

Viruses

Cre-dependent recombinant adeno-associated virus (rAAV) for GCaMP7f (rAAV1-syn-FLEX-jGCaMP7f-WPRE, Addgene #1944820-AAV1, titer: ≥1:10^13 vg/mL) and GCaMP8m ((rAAV1-syn-FLEX-jGCaMP8m-WPRE, Addgene # 162378-AAV1, titer: ≥1:10^13 vg/mL) were used to express GCaMP7f or GCaMP8m in the right, dorsal hippocampus of VIP-Cre mice crossed with Df(16)A$^{+/-}$ mice. The Cre-dependent recombinase enabled expression of calcium sensor GCaMP7f or GCaMP8m in VIP+ interneurons (INs).

Viral injections and hippocampal window/headpost implant

During isoflurane anesthesia, Df(16)A$^{+/-}$ x VIP-cre mice were placed onto a stereotaxic surgery instrument. Meloxicam and bupivacaine were administered subcutaneously to reduce discomfort and provide analgesia. The skin was cut along the midline to expose the skull, and a craniotomy was performed over the right hemisphere with a dental drill. A Nanoject injector was loaded with

a sterile glass capillary filled with mineral oil and rAAV1-syn-FLEX-jGCaMP7f-WPRE or rAAV1-syn-FLEX-jGCaMP8m-WPRE and lowered into dorsal CA1 of the right hemisphere. Injections were made at AP -2.2, ML -1.75, DV - 1.8, -1.6, -1.4, -1.2, -1.1, -1.0, -0.8 relative to bregma with 64 nl of virus injected at each DV level. The pipette was held within the brain for 5 minutes after the last injection and slowly raised from the brain. The skin was sutured, and a topical antibiotic was applied to the suture site. 1.0 mL of saline was subcutaneously given to each mouse, while the mice recovered in their home cage with a heat pad. Four days after viral injection, a circular cannula with a glass window was inserted into the cavity produced by craniotomy as previously described[111]. Similarly as described above, mice were anesthetized with isoflurane and placed on a stereotaxic surgery instrument. Meloxicam and bupivacaine were subcutaneously given to the mice. The skull was exposed, and a 3 mm craniotomy was performed over the right hippocampus at AP -2.2, ML -1.75 relative to bregma, centered around the injection site. After removal of the dura, the cortex was slowly aspirated with negative pressure and the consistent application of ice-cold cortex buffer. When the horizontal fibers over CA1 were exposed, aspiration was stopped and a sterile collagen membrane was applied to stop bleeding. A 3 mm circular cannula with a glass window was placed into the craniotomy and glued into the site with Vetbond. A headpost was then attached to the posterior of the skull with layers of dental cement. 1.0 mL of saline was subcutaneously given to each mouse, while the mice recovered in their home cage with a heat pad. All mice were monitored for 3 days of post-operative care until behavior training began.

Behavioral training and paradigms

Following the post-op recovery period, mice were acclimated to handling and head-fixation for a few days, while being water restricted to 85-90% of their original weight. Mice were trained to run on a fabric, cue-free burlap belt with random rewards that were automatically dispensed at a decreasing number of random locations. Mice were trained for ~1 week on the cue-free belt and then were transitioned to a cue rich belt during the imaging experiments.

Random Foraging Task:

Water restricted mice were imaged on a cue rich familiar belt for 2 days with 3 random rewards distributed across the length of the belt, randomized every lap.

AOD-based two-photon calcium imaging

After the mice were acclimated and trained in the respective tasks, a high-resolution structural Z-stack was captured 24 hours prior to imaging, while the mouse was anesthetized with isoflurane. The reference Z-stack was used to identify the 3D position of the GCaMP-positive neurons for access by the custom-modified AOD (acousto-optic deflector) microscope (Femto3D-ATLAS, Femtomics Ltd). The AOD microscope was used as previously described in Geiller et al. 2020, and Vancura and Geiller et al. 2023.

To provide stable transmission parameters during chronic imaging in the entire 3D scanning volume, the AOD microscope was extended with a high-speed and precision beam stabilization unit, which was directly attached to the AOD scan head, sensitive to input beam misalignment. The beam stabilization unit consisted of two quadrant detectors (PDQ80A and TPA101, Thorlabs)

and two broadband dielectric mirrors (Thorlabs) mounted on motorized mirror mounts (Femtonics). Beam alignment was performed by the LaserControl software (Femtonics).

A water immersion objective (x16 Nikon CF175) was used to focus at the dorsal CA1 pyramidal layer and then fixed in position. A tunable two-photon laser (Coherent Ultra II) was adjusted to wavelength = 920 nm. The high-resolution structural Z-stack was captured in CA1 from ~100 um below to glass to ~500 um to span the entirety of CA1 from the *stratum oriens* to the *stratum lacunosum-moleculare* with a 800x800 pixel capture with a resolution of 1.25 um per pixel with a 4 um step size. Laser power and photomultiplier tube (PMT) detectors (GaAsP, H10770PA-40, Hamamatsu) were compensated in power and gain throughout the Z-stack capture. After the Z-stack was completed, the mouse was returned to its home cage and given 24 hours to recover before functional imaging.

Using the integrated software from Femtonics (MES), the Z-stack was examined, and 100-150 interneurons were manually selected to generate a spreadsheet of the x-y-z positions at the center of each respective cell. These x-y-z positions served as the regions of interest (ROIs) that were then used on subsequent days by the AOD microscope to find the position of the corresponding interneurons. For each day of functional imaging in each mouse, the identical field of view was identified within the CA1 pyramidal layer and then the ROIs were loaded in using the software for AOD 3D imaging. Each imaging session was taken for 10 minutes, with approximately 5-10 Hz for each recording experiment (frame rate depended on the number of ROIs, ROI size, imaging resolution, and scanning speed).

Immunohistochemistry

The immunohistochemical (IHC) staining strategy is consistent with our previously published methods[78,81]. In brief: mice were collected the last day after imaging and perfused with 20 mL Phosphate Buffered Saline (PBS) followed by 20 mL of 4% paraformaldehyde (PFA, Electron Microscopy Sciences) and the brain extracted for overnight fixation in 4% PFA. The next day, the brains were washed 3 x 5 minutes with 1x PBS and subsequently vibratome sliced for horizontal sections from the dorsal side of the brain into 75 µM sections. The relevant sections were then taken through our IHC protocol. Sections were permeabilized for 2 x 20 minutes (0.03% Triton-X 100 (Sigma-Aldrich), 1x PBS), blocked for 45 minutes (0.03% Triton-X 100, 10% Normal Donkey Serum (NDS), 1x PBS), and incubated with primary antibodies (Table 1) for 1 hour at room temperature and overnight at 4 degrees with agitation. After 48 hours, primary antibodies were washed out (3 x 5 minutes 1x PBS) and secondary antibodies were applied for 2 hours (Table 1). Secondary antibodies were removed and the sections were washed with 1x PBS 5 x 15 minutes, and the sections were mounted for confocal imaging.

Cell Marker	Round	Primary Antibody (dilution)	Secondary Antibody (dilution)	Catalog #
Cholecystokinin (CCK)	1	rabbit anti-proCCK (1:500)	donkey anti-rabbit DyLight 405 (1:300)	Frontier Institute CCK-pro-Rb-Af350

Calretinin (CalR)	1	Guinea pig anti-Calretinin (1:1000)	donkey anti-guinea pig Alexa 568 (1:300)	Swant CRgp7
Muscarinic Cholinergic M2 Receptor (M2R)	1	rat anti-M2R (1:2000)	donkey anti-rat Alexa 647 (1:300)	Millipore MAB367

Table 1. Antibodies used in this study

Confocal imaging

The NikonA1 confocal microscope used to take multi-channel fluorescence images (405 nm, 488 nm, 561 nm, and 640 nm excitation for the four blue, green, red and far-red colored channels) of labeled tissue sections. Image capturing yielded 2048 x 2048 pixel z-stacks of the entire depth of the section (with 3 microns between each image of a given stack). Z-stacks were viewable via Fiji (Image J).

Registration of confocal images to *in vivo* z-stacks and identification of immunopositivity/negativity

Unique groupings of cells from *in vivo* z-stacks were used as visual fiducial markers to manually register *ex vivo* 75 μm z-stack images in ImageJ, section by section. Care was taken to note the orientation of the *ex vivo* sections regarding the *in vivo* z-stack images. The coordinates taken from the AOD software when selecting ROIs for imaging against the *in vivo* z-stack were used to identify ROI ID numbers in the registered immunohistochemically stained images.

Assignment of subtype identity based on immunostaining

Interneuron subtypes were assigned based on our previously published classification strategy[78].

Cholecystokinin-expressing basket cells (CCKBCs):
GCaMP-expressing, immunopositive for proCCK, immunonegative for CalR and M2R[112,113]. This population represents perisomatic-targeting basket cells.

Interneuron-selective interneuron type 2 (ISI2s):
GCaMP-expressing, immunonegative for CalR, CCK and M2R. Present in *stratum radiatum* or *stratum lacunosum moleculare* CA1 layers[112,113].

Interneuron-selective interneuron type 3 (ISI3s):
GCaMP-expressing, immunopositive for CalR and immunonegative for CCK and M2R. Present in all CA1 layers[102,112–115].

VIP only (VIPos):
GCaMP-expressing, immunonegative for CalR, CCK and M2R. Present in *stratum oriens* or *stratum pyamidale* CA1 layers. This category excludes CCKBCs, ISI2s, and ISI3s, and could possibly include long-range projecting interneurons[116], but it may not be restricted to them; therefore we called them VIP only for our purposes in this study.

Pre-processing of Ca2+ imaging data

Raw movies of each individual cell were independently motion corrected using the whole-frame cross registration implemented in the SIMA package[117]. ROIs were then hand-drawn over each imaged cell. Fluorescence was extracted from each drawn ROI using SIMA. DeltaF/F was then

computed based on a 1st percentile baseline value over a 30-second rolling window. The DeltaF/F traces were then smoothed through an exponential filter. For analyses involving velocity regressed traces, each animal's velocity was smoothed with a Hanning filter and then covariate linear regression was applied to each fluorescence trace where the smoothed velocity is regressed out.

Velocity Correlation

For each cell, velocity correlation was computed by taking Pearson's correlation coefficient between the DeltaF/F trace and animal's smoothed velocity with a -5 second to +5 second rolling lag. The highest absolute value of the correlation coefficients in this time window was taken as the correlation coefficient for the respective cell.

Peri-Event Time Averages (PETA)

For salient stimuli such as reward distribution events, a PETA was constructed around each event respectively. These events were z-score and then averaged for each respective cell, and the z-scored averages were visualized using a heatmap or an averaged line-plot. A Post-Pre metric was calculated based on the z-scored averages as a measure for event modulation.

Spatial Tuning Curve

The 2 meter belt was divided into 100 bins (~2cm per bin). Spatial tuning curves for each cell during an experiment were generated by averaging the velocity regressed DeltaF/F in each bin, when the animal was running over 5 cm/s.

Place field calculation

The spatial tuning curves were shuffled 1000 times by circularly rotating the velocity-regressed $\Delta F/F$ tuning curves around the 100 spatial bins to generate a shuffle distribution. Cells were classified as being spatially selective (i.e., having a place field) if the cell's tuning curve exceeded the 95th percentile (or was under the 5th percentile for negatively selective cells) with at least 10 sequential bins over/under the cutoffs from the shuffled distribution. The number of bins over or under the 95th and 5th percentile curves were visualized and a cutoff of 30 consecutive bins was used for the figures as it represented the approximate 75th quartile for place field width.

Position Decoding

A linear classifier support vector machine (SVM) was trained on the tuning curves of each respective cell and the decoding error was visualized. The SVM was cross-validated by training the classifier on (n-1) laps and evaluating on the held-out lap and this process was repeated such that every lap was utilized as a test lap at least once. Furthermore, the SVM was bootstrapped with different numbers of input cells and input laps to compare the position decoding efficacy between genotypes.

Cross-correlation Analysis

Pairwise Pearson's correlation coefficients were computed for every pair of cells within a given experiment. The average coefficient value for each subtype was then calculated per trial pair and averaged across mice.

Transient Analysis

Online Active Set method to Infer Spikes (OASIS) was used to generate deconvolved spike events based on transient events within the dF/F traces[90]. We understand that these are not true spiking events, and we are using OASIS to algorithmically identify transient events rather than interpret the deconvolved spiking events.

Frequency: The deconvolved events were filtered to remove events that were within 10 frames. The total number of filtered deconvolved events by OASIS was normalized by the total duration of the recording.

For each cell, the average transient was segmented within a 15-second time window and computed by averaging along aligned deconvolved spike times. If multiple detected events were within 10 frames, the events were treated as a single transient. A cell was only used if there were at least 3 detected transients within the total trace to exclude cells without obvious GCaMP-Ca^{2+} dynamics. For each average transient, we computed the median value based on 5 seconds pre peak transient and the range 5-10 seconds after the peak transient (given that the average transient took significantly less than 5 seconds to resolve) to act as the baseline.

Amplitude: The difference between the max value of the average transient and the baseline value was computed

QUANTIFICATION AND STATISTICAL ANALYSIS

Statistical analyses

Subtype comparisons were conducted using one-way ANOVA tests with Tukey's range tests with correction for multiple testing if appropriate. For comparisons across genotypes, unpaired t tests were utilized if the data followed a normal distribution. Otherwise, for non-normally distributed comparisons, the Mann-Whitney U test was used. *, $P < 0.05$, **, $P < 0.01$, ***, $P < 0.001$. All data analysis and visualization were done with custom software built on Python version 2.7.15.

Code and Data availability:

All data used in this report are publicly available. ASD genes and mutations counts can be found in Supplementary table from Zhou et al[2]. SCZ genes and mutation counts can be found in Supplementary table from Singh et al[1]. DD/ID genes and mutations counts can be found in Supplementary table from Kaplanis et al[45]. Genes implicated in UKBB adult cognitive functions can be found in Supplementary table from Chen et al[57]. Genes in 22q11.2 3MB deletion and 1.5 MB deletion can be found in Karayiorgou et al[10]. Human brain cell atlas can be found (https://cellxgene.cziscience.com/collections/283d65eb-dd53-496d-adb7-7570c7caa443). Individual genetics and phenotypic data used in our study from the SPARK project are available through the Simons Foundation (https://base.sfari.org) following the access procedures described in Zhou et al.

The code used for our implementation of the Cell type bias with analysis pipeline, and code to generating all figures and tables, is available on GitHub: (https://github.com/explorerwjy/CellTypeBias_VIP.git)

Acknowledgements

S.A.H. is supported by the Burroughs Welcome grant. This work has been supported by the grants NIMHR01MH124923 to D.V. and J.A.G, NIMHR01MH124047 to J.A.G, Stavros Niarchos Foundation to J.A.G., and NIMHR01MH124047 NIMHR01MH124867 NINDSR01NS133381 to A.L. We thank members of the Gogos, Losonczy, and Vitkup labs for fruitful scientific discussions.

Author Contributions

S.H., J.W., J.A.G., A.L., and D.V. conceived the study. J.W. and J.C. performed genetic bias and computational analyses. S.H. and B.R. collected and analyzed experimental data. S.H., J.W., J.A.G., A.L., and D.V. wrote the manuscript.

Supplemental Figures

Figure	Statistics
5C	*CCKBC:* CCK basket cells student's t-test: T statistic: -1.313, P = 0.019. *ISI3*: Interneuron-Selective Interneuron Type 3: Student's T test Statistic: -3.284, P = 0.001. *ISI2:* Interneuron-Selective Interneuron Type 2: Student's T test Statistic: 2.191, P = 0.030. *VIP+ Alone:* Student's T-test Statistic: 1.105, P = 0.269
5E	Mann-Whitney test, t = 104931.0, P = 4.1530e-05.
5G	Mann-Whitney test, t =24290.0, P = 0.0388.
5I	Mann-Whitney test, t = 42011.0, P = 2.5817e-13.
5J	Mann-Whitney test, t = 54521.5, P = 0.0013
5L	*CCKBC*: cholecystokinin-expressing basket cells Mann-Whitney U test: P = 0.292, *ISI3*: interneuron-selective interneuron type 3 cells Mann-Whitney U test: P = 0.0029, *ISI2*: interneuron-selective interneuron type 2 cells Mann-Whitney U test: P = 0.0026, *VIP-Alone*: Mann-Whitney U test: P = 0.036. For Mann Whitney U tests: median ± inter-quartile range.
6A	Averaged per animal: Mann-Whitney U test: statistic = 3.5, P = 0.144
6B	10 cells: Mann-Whitney U test: P = 6.67e-10, 30 cells: Mann-Whitney U test: P = 8.32e-11, 50 cells: Mann-Whitney U test: P = 2.75e-16, 70 cells: Mann-Whitney U test: P = 2.67e-18, 90 cells: Mann-Whitney U test: P = 3.00e-21.
6C	5 laps: Mann-Whitney U test: P = 2.66e-6, 10 laps: Mann-Whitney U test: P =2.27e-21, 15 laps: Mann-Whitney U test: P =2.49e-15.
6D	0 fields: Mann-Whitney U test: p = 0.056, 1 field: Mann-Whitney U test: P = 0.030, 2 fields: Mann-Whitney U test: P = 0.097, 3 fields: Mann-Whitney U test: P = 0.062.
6F	Welch's T-test comparisons: ISI2 vs VIPo: P = 0.0067. ISI3 vs ISI3: P = 0.043. ISI3 vs VIPo: P = 0.039. VIPo vs ISI2: P = 0.0068. VIPo vs ISI3: P = 0.038. Welch's T-test.

Supplementary Table 1: Statistical detail summary.
Boxplots show the 25th, 50th (median), and 75th quartile ranges, with the whiskers extending to 1.5 interquartile ranges below or above the 25th or 75th quartiles, respectively. Outliers are defined as values extending beyond. the whisker ranges. For Welch's t tests: mean ± sem. For Mann Whitney U tests: median ± inter-quartile range. n.s.: not significant. *: P < 0.05. **: P < 0.01. ***: P < 0.001.

Supplementary Table 2: Human brain Cell type biases (cluster level) for psychiatric disorders.

Supplementary Table 3: Human brain Cell type biases (supercluster level) for psychiatric disorders.

Supplementary Table 4: Human brain differential biases for psychiatric disorders.

Supplementary Table 5: PBS values for ASD FSIQ.

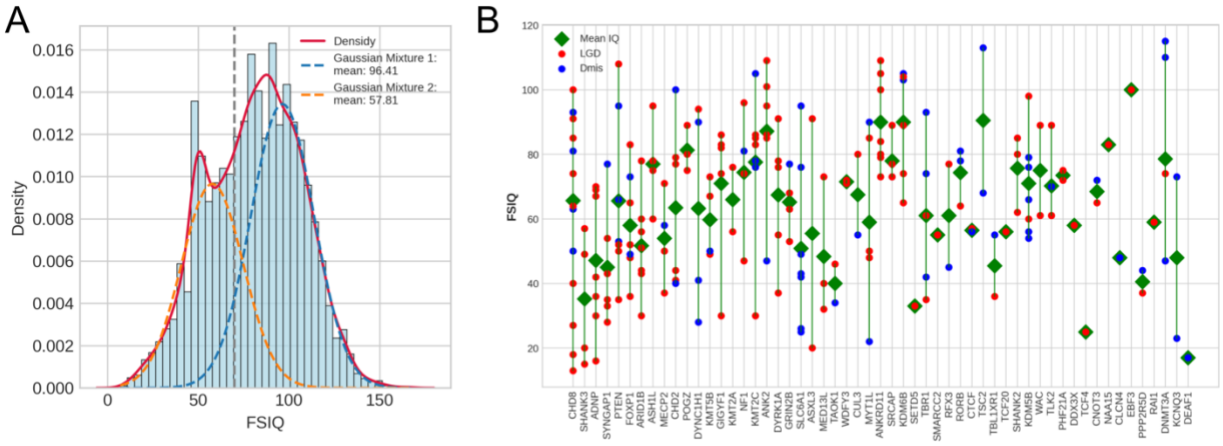

Supplemental Figure 1: Full-scale IQ distribution among ASD probands in the SPARK and ASC cohorts. A). The distribution of FSIQ scores among ASD probands from the SPARK and ASC cohorts. The histogram (blue bars) shows the FSIQ distribution with an overlaid density plot (red line). A two-component Gaussian mixture model was fitted to the data (blue and orange dashed curves), revealing the distinct subpopulations within the FSIQ distribution. The vertical dashed line at FSIQ = 70 indicates a frequently used threshold for intellectual disability (IQ < 70). FSIQ phenotype data was obtained from Zhou *et al*.[2] and Satterstrom *et al*.[58] **B).** Gene-specific FSIQ patterns across the top 61 high-confidence ASD genes, represented by vertical lines. Individual probands are represented as dots, colored by the mutation type, with likely gene-disrupting (LGD) mutations in red and damaging missense (Dmis) mutations in blue. The green diamonds indicate the average FSIQ in the cohorts for each gene. Genes are arranged along the x-axis in based on *de novo* west P-values from Zhou *et al*.[2].

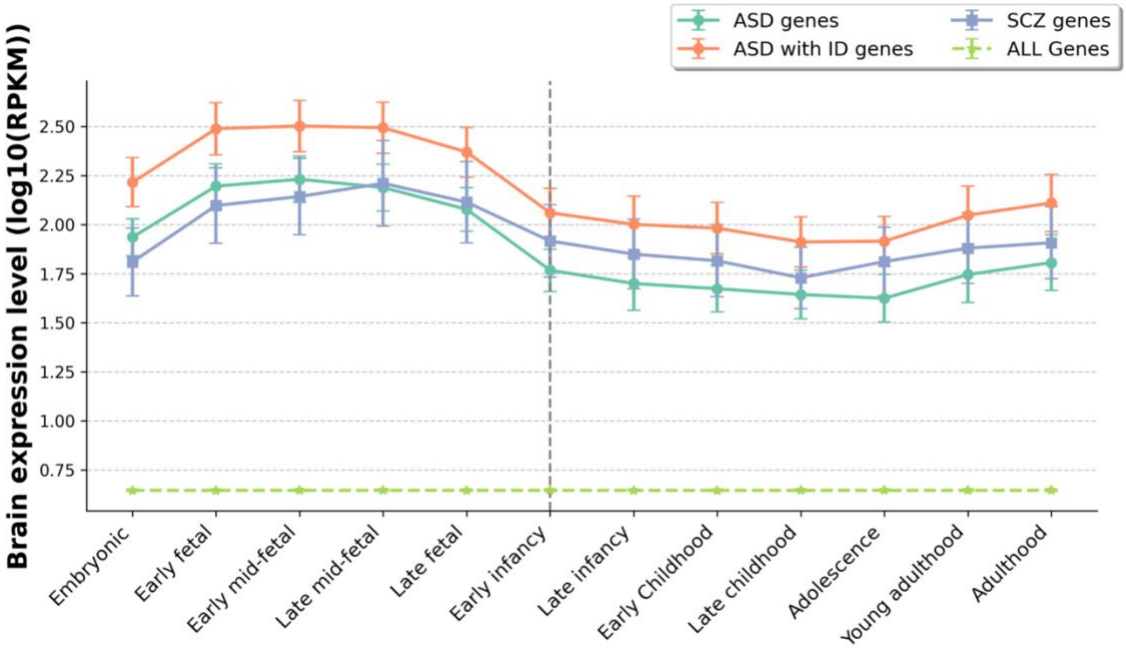

Supplemental Figure 2. Temporal expression patterns of disorder-associated genes across human brain development. Average expression levels (log10 RPKM) of genes associated with different disorders across human brain developmental stages, from embryonic to adult periods. Gene sets include ASD genes (green), ASD with ID genes (orange), SCZ genes (blue), and background genes (dashed yellow). Error bars represent standard error of the mean. SCZ genes show similar prenatal expression level as ASD genes while ASD with ID genes show higher prenatal expression level. The vertical dashed line marks the transition from prenatal to postnatal periods. Expression data derived from the BrainSpan Atlas of Human Brain Development[118].

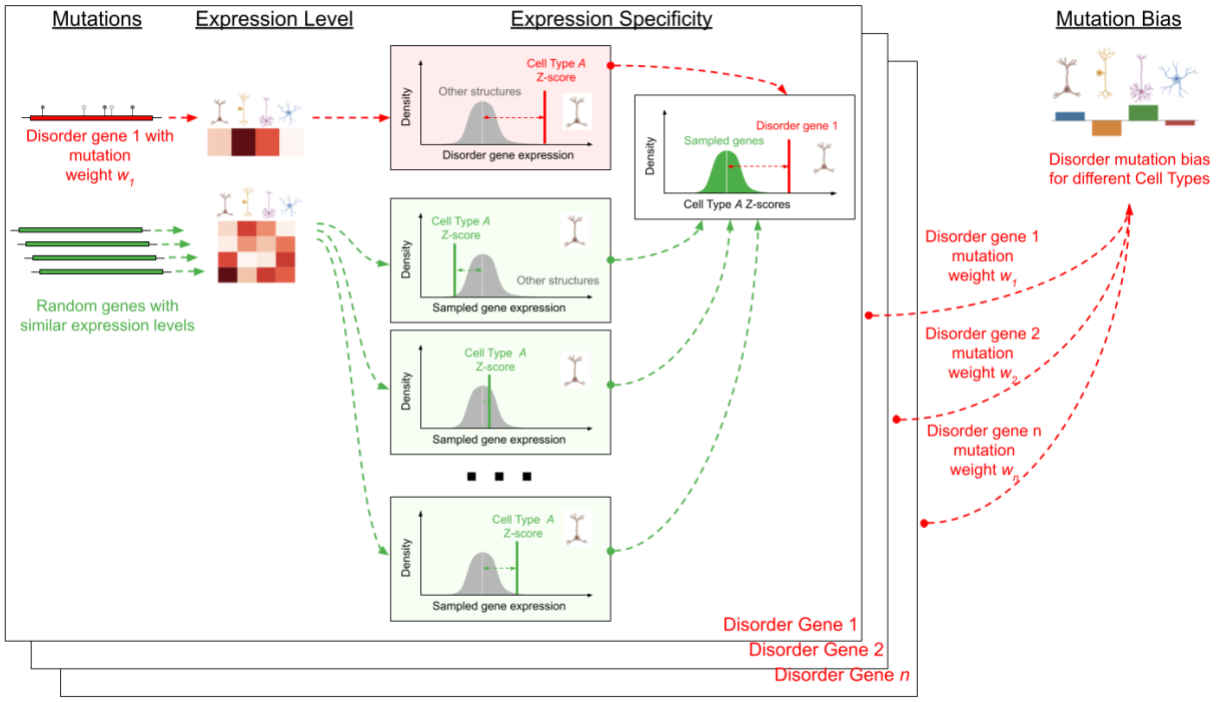

Supplemental Figure 3: Illustration of disorder cell type mutation bias. Illustration of the gene expression analysis used to determine disorder mutation biases for each cell type. To calculate the biases, gene expression specificities were first calculated for each gene and for each cell type in the brain; the expression specificity of a gene in a brain cell type was calculated as the Z-score between the gene expression level in the cell type compared to the distribution of the gene expression levels in the whole brain (sum of UMI cross all cell). The specificities were calculated for each disorder gene (red) and for randomly matched genes (green) with similar expression levels in the brain. For each cell type, expression biases were then calculated for each disorder gene as the Z-score between the expression specificity of that gene and the distribution of expression specificities of random genes with similar expression level in the brain. Based on gene expression biases, disorder mutation biases were determined for each cell type by computing a weighted average of mutation biases across all disorder genes; Gene weights were based on disorder mutation contribution from each gene (see Methods).

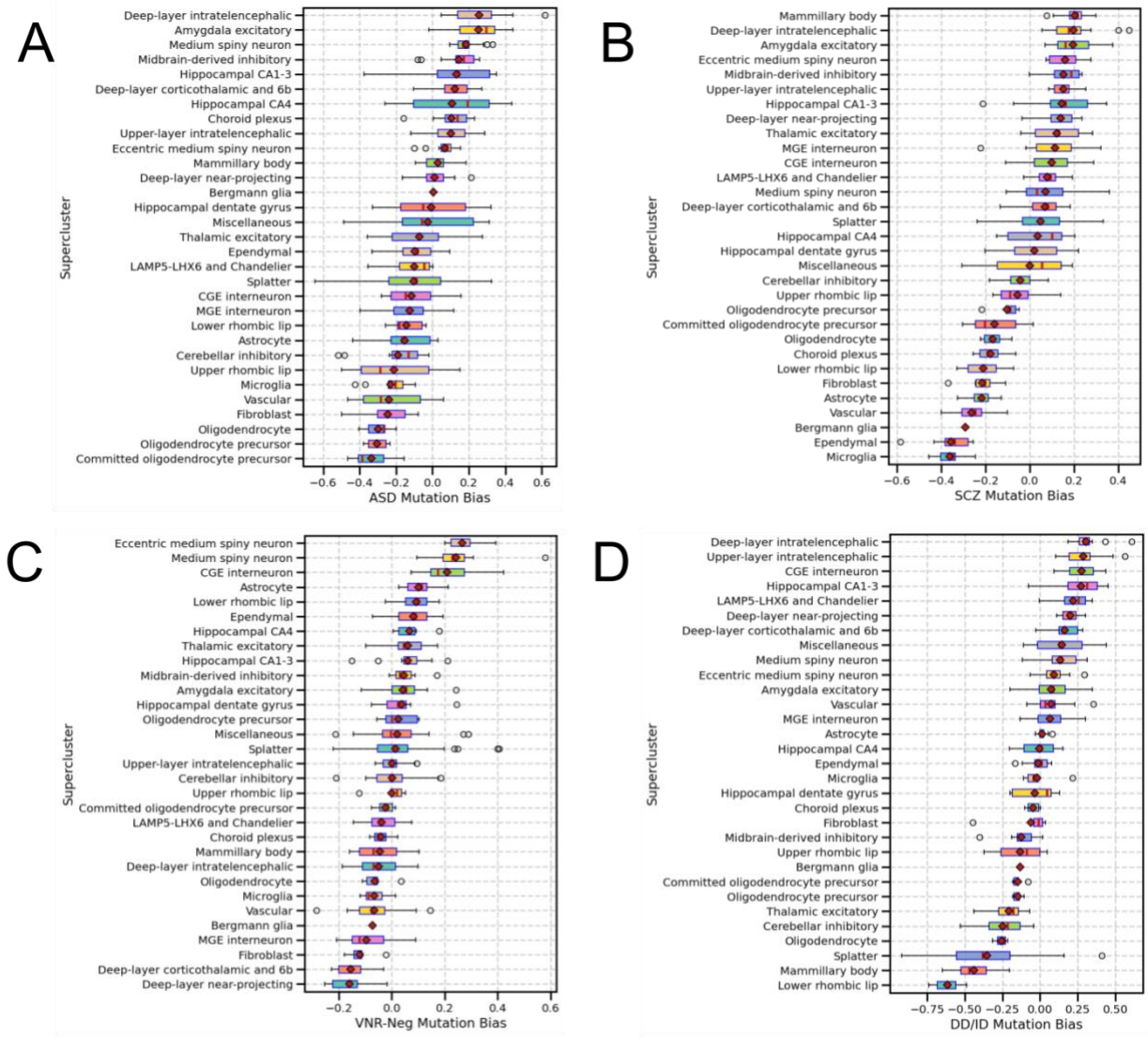

Supplemental Figure 4. Comprehensive analysis of mutation biases across brain cell types in psychiatric disorders. Box plots showing mutation biases for all major brain cell types (superclusters) in **A.)** ASD (top left), **B.)** SCZ (top right), **C)**. VNR Negative genes (bottom left), and **D.)** DD/ID (bottom right). Each bar represents the bias distribution of the human adult brain neuron type belonging to a supercluster, X-axis shows the magnitude of biases. Red diamond shows average bias of each supercluster, red vertical line shows medium bias of each supercluster. Detailed data can be found in Supplementary table 2.

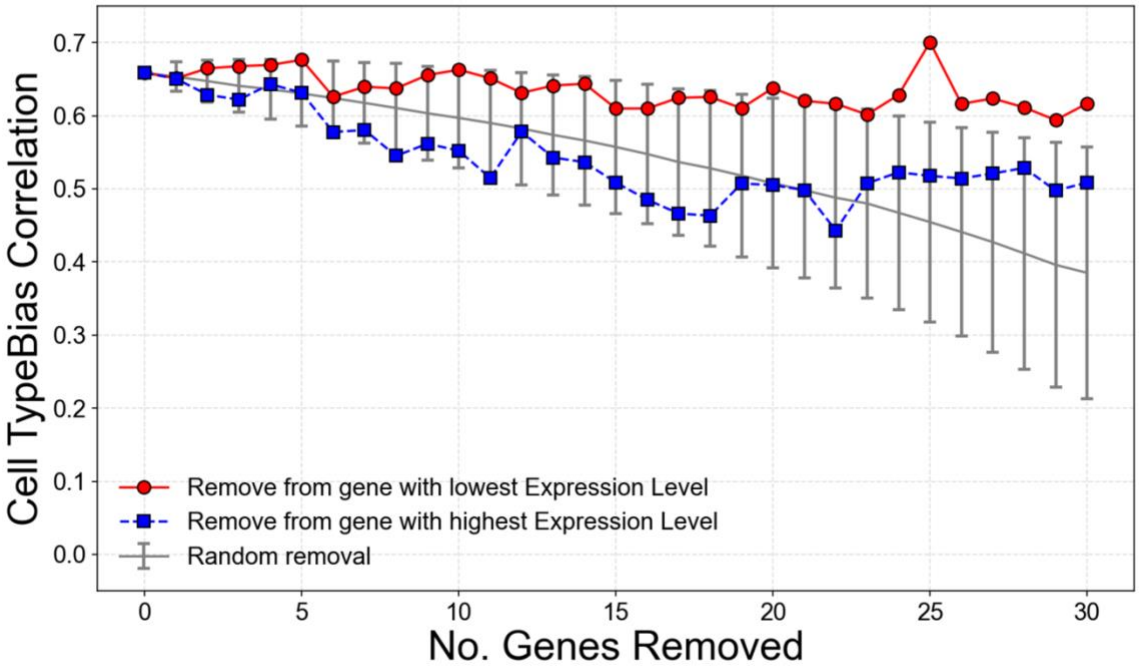

Supplemental Figure 5. Impact of gene expression levels on ASD-SCZ cell type bias correlation. Effect of sequentially removing genes based on their expression levels on the cell type mutation bias correlation between ASD and SCZ. Red line shows correlation changes when removing genes with lowest expression levels first, while blue dashed line shows removal of highest expressing genes first. Grey line and error bars show mean ± standard deviation for random gene removal. The correlation remains relatively stable when removing lowly expressed genes or highly expressed genes. This suggests gene expression levels play a secondary role in determining shared cell type patterns between disorders compared to gene constraint.

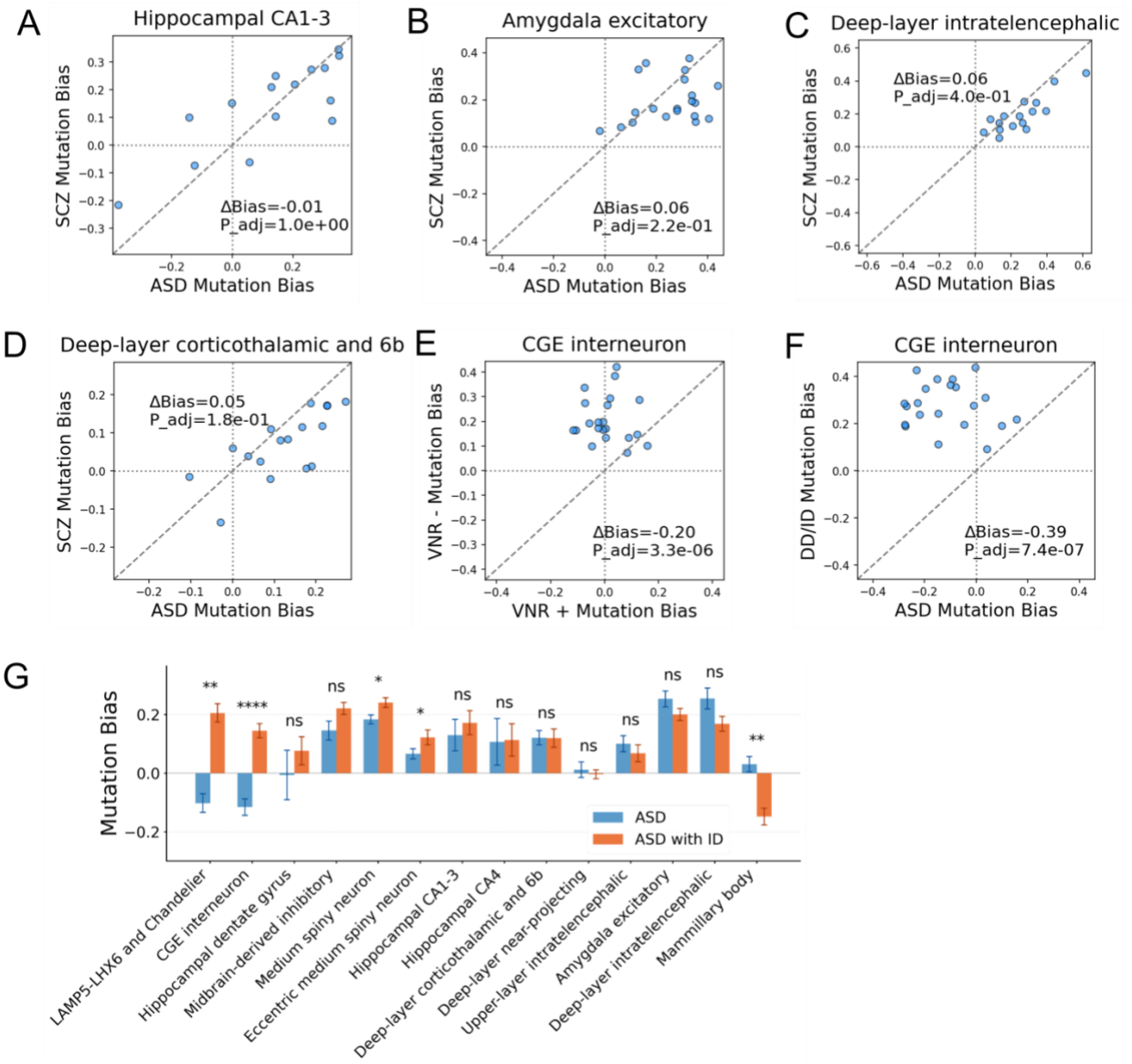

Supplemental Figure 6. ASD and SCZ Mutation bias towards different superclusters. A-D. Detailed comparison of mutation biases in specific neuron superclusters, P-value was calculated based on Wilcoxon signed-rank test with FDR correction: **(A)** Hippocampal CA1-3 neurons show similar bias in ASD and SCZ. **(B)** Amygdala excitatory neurons show similar bias in ASD and SCZ. **(C)** Deep-layer IT neurons show similar bias in ASD and SCZ. **(D)** Deep-layer corticothalamic and 6b neurons show similar bias in ASD and SCZ. **(E)** CGE interneurons show stronger bias in VNR- genes compared to VNR+ genes (adjusted P =3.7e-06). **(F)** CGE interneurons show stronger bias in DD/ID genes compared to ASD genes (adjusted P =1.4e-07). **(G)** Bar plot comparing mutation biases across major neuron types between ASD (blue) and ASD with ID (orange). Asterisks indicate significance level between groups (*: P < 0.05. **: P < 0.01. ***: P < 0.001, ****: P < 0.0001, ns=not significant). Neuron types showing positive mutation bias from at least one disorder are displayed and sorted by bias difference between ASD and ASD with ID. Error bars represent standard error across clusters from corresponding superclass. Detailed data can be found in Supplementary table 4.

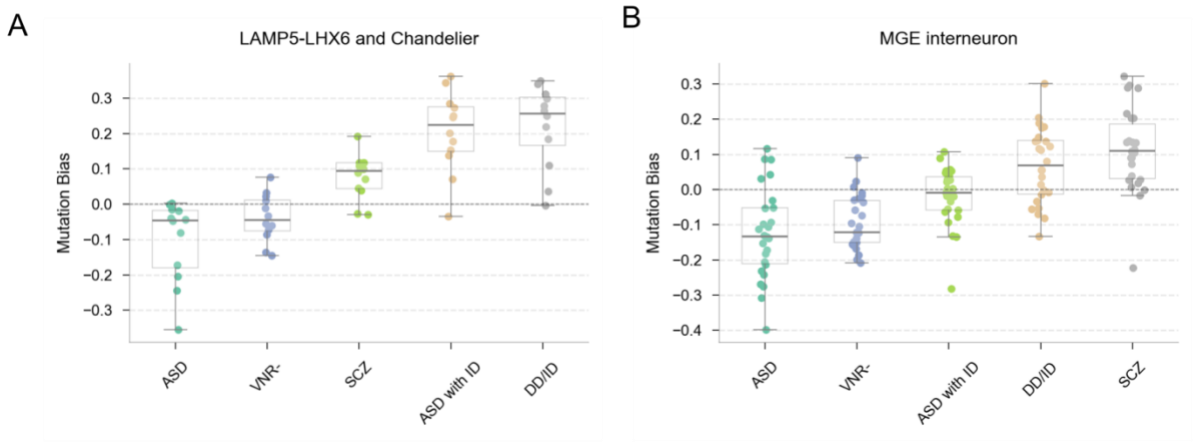

Supplemental Figure 7. Mutation bias comparison across psychiatric disorders for LAMP5-LHX6/Chandelier and MGE interneurons. A: Mutation bias distribution for LAMP5-LHX6 and Chandelier cells across different cohorts: ASD (Mean Bias = -0.10, adjusted P = 1), ASD with ID (Mean Bias = 0.2, adjusted P = 4.0e-04), SCZ (Mean Bias = 0.07, adjusted P = 0.7), VNR- (Mean Bias = -0.03, adjusted P = 1), and DD/ID (Mean Bias = 0.22, adjusted P = 1.0e-03). **B:** Mutation bias distribution for MGE interneurons across different cohorts: ASD (Mean Bias = -0.12, adjusted P = 1), ASD with ID (Mean Bias = 0.02, adjusted P = 1), SCZ (Mean Bias = 0.11, adjusted P = 0.047), VNR- (Mean Bias = -0.1, adjusted P = 1), and DD/ID (Mean Bias = 0.06, adjusted P = 0.1). Detailed data can be found in Supplementary table 2 and 3.

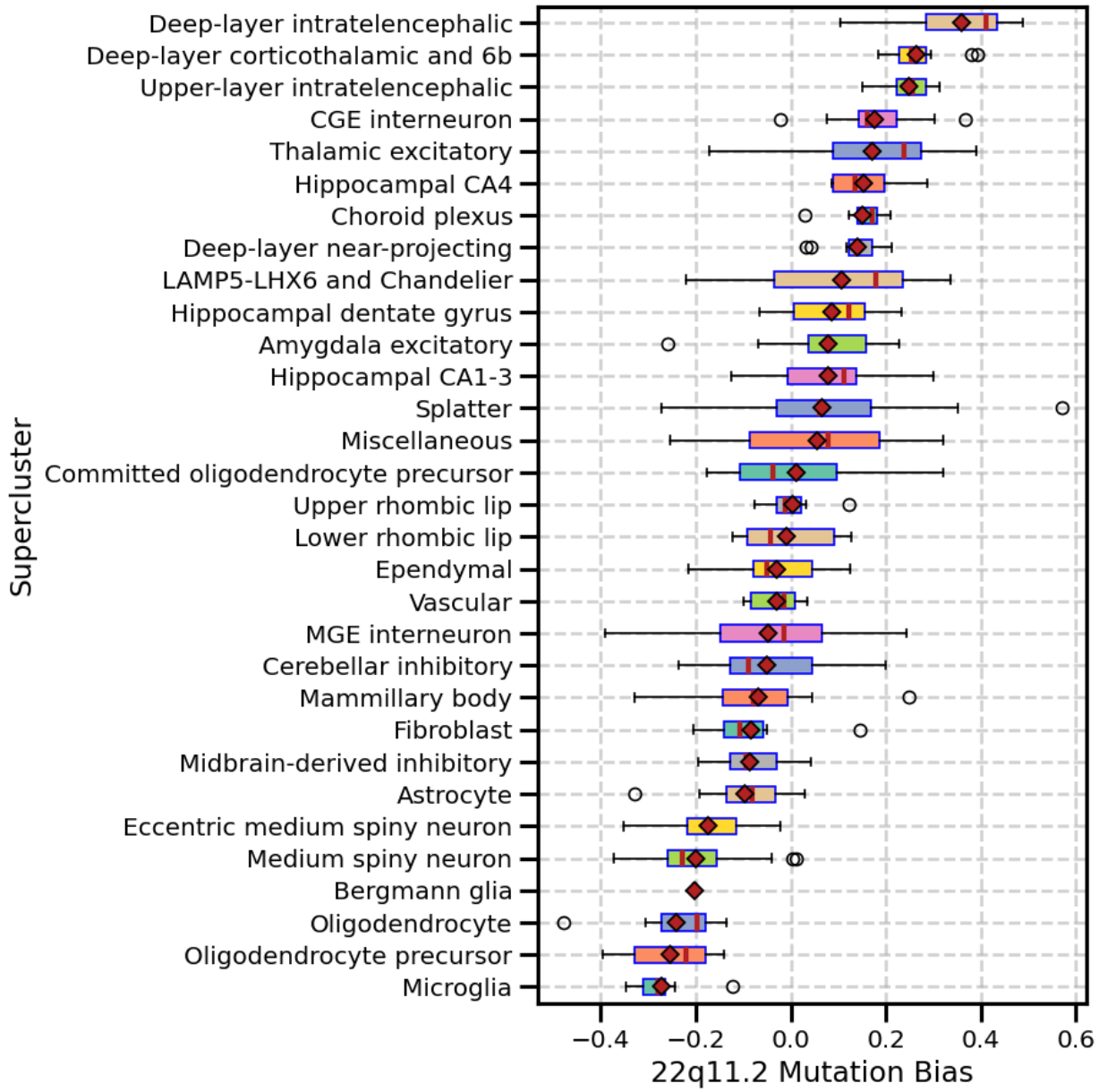

Supplemental Figure 8. Comprehensive analysis of mutation biases across brain cell types in 22q11.2 deletion. Box plots showing mutation biases for all major brain cell types (superclusters). Each bar represents the bias distribution of the human adult brain neuron type belonging to a superclass, X-axis shows the magnitude of biases. Red diamond shows average bias of each supercluster, red vertical line shows medium bias of each supercluster. Detailed data can be found in Supplementary table 2 and 3.

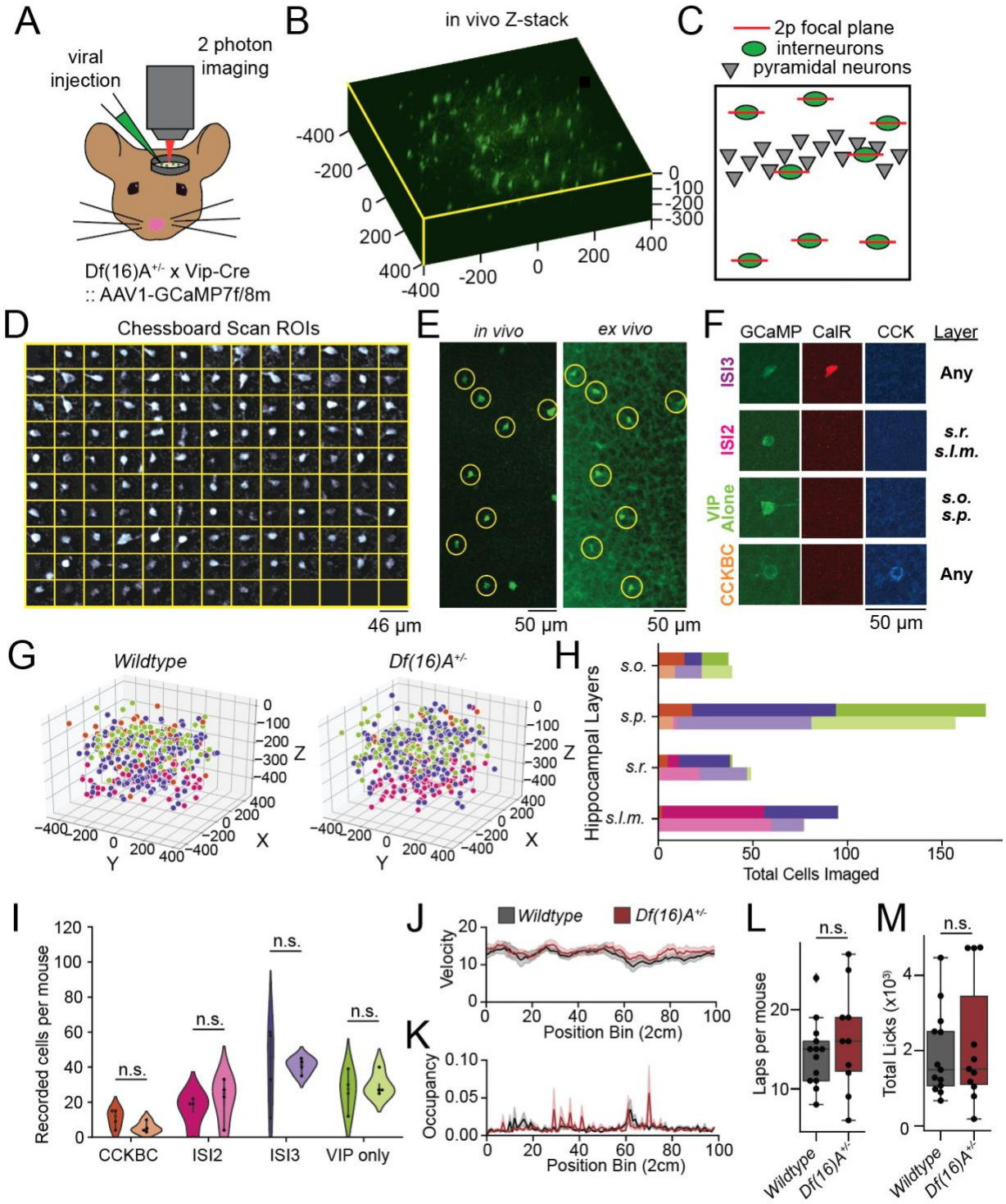

Supplemental Figure 9. VIP+ Cell imaging and targeting strategy.

A. Schematic for mouse crossing and viral injection and calcium imaging setup. **B.** 3D reconstruction of Z-stack from VIP-cre mice **C.** Schematic of 3D regions of interest (ROIs) imaged with AOD 2-photon microscopy. **D.** Example chessboard scan view of imaged ROIs. **E.** Manual registration of *in vivo* Z-stack section with *ex vivo* 75 µm transverse section for *post hoc* subtype classification with immunohistochemistry. **F.** Histological strategy for defining VIP-expressing cell subtypes. **G.** 3D distribution of all cells imaged from both genotypes. **H.** Distribution of VIP+ subtypes

across CA1 hippocampal layers. **I.** Number of cells recorded per mouse (n=4, ISI3: ISI2: VIP+ Alone: CCKBC:). **J.** Average velocity in cm per second plotted by location on the belt of WT (black) and *Df(16)A*$^{+/-}$ (brown) mice. **K.** Average percent occupancy on the belt by position per genotype plotted by location on the belt of WT (black) and *Df(16)A*$^{+/-}$ (brown) mice. **L.** Total laps across mice within genotype (WT: 14.4 ± 1.1 laps, *Df(16)A*$^{+/-}$: 16.2 ± 2.0 laps, Mann Whitney U = 51.5, P = 0.21). **M**. Licking proportion of WT (black) and *Df(16)A*$^{+/-}$ (brown). There is no significant difference in total licks across the belt during Random Foraging in WT (n = 4) or *Df(16)A*$^{+/-}$ (n = 4) depicted by box-and-whisker plot, WT: 1916 ± 304 licks, *Df(16)A*$^{+/-}$: 2200 ± 489 licks, Mann-Whitney U Test, P = 0.408.

References

1. Singh, T., Poterba, T., Curtis, D., Akil, H., Al Eissa, M., Barchas, J.D., Bass, N., Bigdeli, T.B., Breen, G., Bromet, E.J., et al. (2022). Rare coding variants in ten genes confer substantial risk for schizophrenia. Nature *604*, 509–516.

2. Zhou, X., Feliciano, P., Shu, C., Wang, T., Astrovskaya, I., Hall, J.B., Obiajulu, J.U., Wright, J.R., Murali, S.C., Xu, S.X., et al. (2022). Integrating de novo and inherited variants in 42,607 autism cases identifies mutations in new moderate-risk genes. Nat. Genet. *54*, 1305–1319.

3. Gilman, S.R., Chang, J., Xu, B., Bawa, T.S., Gogos, J.A., Karayiorgou, M., and Vitkup, D. (2012). Diverse types of genetic variation converge on functional gene networks involved in schizophrenia. Nat. Neurosci. *15*, 1723–1728.

4. Gilman, S.R., Iossifov, I., Levy, D., Ronemus, M., Wigler, M., and Vitkup, D. (2011). Rare de novo variants associated with autism implicate a large functional network of genes involved in formation and function of synapses. Neuron *70*, 898–907.

5. Gandal, M.J., Haney, J.R., Parikshak, N.N., Leppa, V., Ramaswami, G., Hartl, C., Schork, A.J., Appadurai, V., Buil, A., Werge, T.M., et al. (2018). Shared molecular neuropathology across major psychiatric disorders parallels polygenic overlap. Science *359*, 693–697.

6. Rees, E., Creeth, H.D.J., Hwu, H.-G., Chen, W.J., Tsuang, M., Glatt, S.J., Rey, R., Kirov, G., Walters, J.T.R., Holmans, P., et al. (2021). Schizophrenia, autism spectrum disorders and developmental disorders share specific disruptive coding mutations. Nat. Commun. *12*, 5353.

7. Trevisan, D.A., Foss-Feig, J.H., Naples, A.J., Srihari, V., Anticevic, A., and McPartland, J.C. (2020). Autism spectrum disorder and schizophrenia are better differentiated by positive symptoms than negative symptoms. Front. Psychiatry *11*, 548.

8. Spek, A.A., and Wouters, S.G.M. (2010). Autism and schizophrenia in high functioning adults: Behavioral differences and overlap. Res. Autism Spectr. Disord. *4*, 709–717.

9. Schneider, M., Debbané, M., Bassett, A.S., Chow, E.W.C., Fung, W.L.A., van den Bree, M., Owen, M., Murphy, K.C., Niarchou, M., Kates, W.R., et al. (2014). Psychiatric disorders from childhood to adulthood in 22q11.2 deletion syndrome: results from the International Consortium on Brain and Behavior in 22q11.2 Deletion Syndrome. Am. J. Psychiatry *171*, 627–639.

10. Karayiorgou, M., Simon, T.J., and Gogos, J.A. (2010). 22q11.2 microdeletions: linking DNA structural variation to brain dysfunction and schizophrenia. Nature Reviews Neuroscience 2010 11:6 *11*, 402–416.

11. Rees, E., Kendall, K., Pardiñas, A.F., Legge, S.E., Pocklington, A., Escott-Price, V., MacCabe, J.H., Collier, D.A., Holmans, P., O'Donovan, M.C., et al. (2016). Analysis of intellectual disability copy number variants for association with schizophrenia. JAMA Psychiatry *73*, 963–969.

12. Miller, D.T., Adam, M.P., Aradhya, S., Biesecker, L.G., Brothman, A.R., Carter, N.P., Church, D.M., Crolla, J.A., Eichler, E.E., Epstein, C.J., et al. (2010). Consensus statement:

chromosomal microarray is a first-tier clinical diagnostic test for individuals with developmental disabilities or congenital anomalies. Am. J. Hum. Genet. *86*, 749–764.

13. Ropers, H.H. (2008). Genetics of intellectual disability. Curr. Opin. Genet. Dev. *18*, 241–250.

14. Vissers, L.E.L.M., Gilissen, C., and Veltman, J.A. (2016). Genetic studies in intellectual disability and related disorders. Nat. Rev. Genet. *17*, 9–18.

15. Harvey, P.D., and Strassnig, M. (2012). Predicting the severity of everyday functional disability in people with schizophrenia: cognitive deficits, functional capacity, symptoms, and health status. World Psychiatry *11*, 73–79.

16. Bowie, C.R., and Harvey, P.D. (2006). Cognitive deficits and functional outcome in schizophrenia. Neuropsychiatr. Dis. Treat. https://doi.org/10.2147/nedt.s24531.

17. Bowie, C.R., Reichenberg, A., Patterson, T.L., Heaton, R.K., and Harvey, P.D. (2006). Determinants of real-world functional performance in schizophrenia subjects: Correlations with cognition, functional capacity, and symptoms. Am. J. Psychiatry *163*, 418–425.

18. Millan, M.J., Agid, Y., Brüne, M., Bullmore, E.T., Carter, C.S., Clayton, N.S., Connor, R., Davis, S., Deakin, B., DeRubeis, R.J., et al. (2012). Cognitive dysfunction in psychiatric disorders: characteristics, causes and the quest for improved therapy. Nat. Rev. Drug Discov. *11*, 141–168.

19. Trubetskoy, V., Pardiñas, A.F., Qi, T., Panagiotaropoulou, G., Awasthi, S., Bigdeli, T.B., Bryois, J., Chen, C.Y., Dennison, C.A., Hall, L.S., et al. (2022). Mapping genomic loci implicates genes and synaptic biology in schizophrenia. Nature *604*, 502–508.

20. Bryois, J., Skene, N.G., Hansen, T.F., Kogelman, L.J.A., Watson, H.J., Liu, Z., Eating Disorders Working Group of the Psychiatric Genomics Consortium, International Headache Genetics Consortium, 23andMe Research Team, Brueggeman, L., et al. (2020). Genetic identification of cell types underlying brain complex traits yields insights into the etiology of Parkinson's disease. Nat. Genet. *52*, 482–493.

21. Duncan, L.E., Li, T., Salem, M., Li, W., Mortazavi, L., Senturk, H., Shahverdizadeh, N., Vesuna, S., Shen, H., Yoon, J., et al. (2025). Mapping the cellular etiology of schizophrenia and complex brain phenotypes. Nat. Neurosci., 1–11.

22. Yao, S., Harder, A., Darki, F., Chang, Y.-W., Li, A., Nikouei, K., Volpe, G., Lundström, J.N., Zeng, J., Wray, N., et al. (2024). Connecting genomic results for psychiatric disorders to human brain cell types and regions reveals convergence with functional connectivity. medRxiv. https://doi.org/10.1101/2024.01.18.24301478.

23. Broglio, C., Martín-Monzón, I., Ocaña, F.M., Gómez, A., Durán, E., Salas, C., and Rodríguez, F. (2015). Hippocampal pallium and map-like memories through vertebrate evolution. J. Behav. Brain Sci. *05*, 109–120.

24. Rodríguez, F., López, J.C., Vargas, J.P., Broglio, C., Gómez, Y., and Salas, C. (2002). Spatial memory and hippocampal pallium through vertebrate evolution: insights from reptiles and teleost fish. Brain Res. Bull. *57*, 499–503.

25. Buzsáki, G. (2002). Theta oscillations in the hippocampus. Neuron *33*, 325–340.

26. Pelkey, K.A., Vargish, G.A., Pellegrini, L.V., Calvigioni, D., Chapeton, J., Yuan, X., Hunt, S., Cummins, A.C., Eldridge, M.A.G., Pickel, J., et al. (2023). Evolutionary conservation of hippocampal mossy fiber synapse properties. Neuron *111*, 3802-3818.e5.

27. Hamm, J.P., Peterka, D.S., Gogos, J.A., and Yuste, R. (2017). Altered Cortical Ensembles in Mouse Models of Schizophrenia. Neuron *94*, 153-167.e8.

28. Herrlinger, S.A., Rao, B.Y., Conde Paredes, M.E., Tuttman, A.L., Arain, H., Varol, E., Gogos, J.A., and Losonczy, A. (2024). Disorganized Inhibitory Dynamics and Functional Connectivity in Hippocampal area CA1 of 22q11.2 Deletion Mutant Mice. bioRxiv, 2024.04.28.591464. https://doi.org/10.1101/2024.04.28.591464.

29. Gogos, J.A., Crabtree, G., and Diamantopoulou, A. (2020). The abiding relevance of mouse models of rare mutations to psychiatric neuroscience and therapeutics. Schizophr. Res. *217*, 37–51.

30. Diamantopoulou, A., and Gogos, J.A. (2019). Neurocognitive and Perceptual Processing in Genetic Mouse Models of Schizophrenia: Emerging Lessons. Neuroscientist *25*, 597–619.

31. Arguello, P.A., and Gogos, J.A. (2006). Modeling madness in mice: one piece at a time. Neuron *52*, 179–196.

32. Gordon, A., Forsingdal, A., Klewe, I.V., Nielsen, J., Didriksen, M., Werge, T., and Geschwind, D.H. (2019). Transcriptomic networks implicate neuronal energetic abnormalities in three mouse models harboring autism and schizophrenia-associated mutations. Molecular Psychiatry 2019 26:5 *26*, 1520–1534.

33. Siletti, K., Hodge, R., Mossi Albiach, A., Lee, K.W., Ding, S.-L., Hu, L., Lönnerberg, P., Bakken, T., Casper, T., Clark, M., et al. (2023). Transcriptomic diversity of cell types across the adult human brain. Science *382*, eadd7046.

34. Geschwind, D.H., and Flint, J. (2015). Genetics and genomics of psychiatric disease. Science *349*, 1489–1494.

35. Iossifov, I., O'Roak, B.J., Sanders, S.J., Ronemus, M., Krumm, N., Levy, D., Stessman, H.A., Witherspoon, K.T., Vives, L., Patterson, K.E., et al. (2014). The contribution of de novo coding mutations to autism spectrum disorder. Nature *515*, 216–221.

36. Matson, J.L., and Shoemaker, M. (2009). Intellectual disability and its relationship to autism spectrum disorders. Res. Dev. Disabil. *30*, 1107–1114.

37. Woodberry, K.A., Giuliano, A.J., and Seidman, L.J. (2008). Premorbid IQ in schizophrenia: a meta-analytic review. Am. J. Psychiatry *165*, 579–587.

38. Khandaker, G.M., Barnett, J.H., White, I.R., and Jones, P.B. (2011). A quantitative meta-analysis of population-based studies of premorbid intelligence and schizophrenia. Schizophr. Res. *132*, 220–227.

39. Creeth, H.D.J., Rees, E., Legge, S.E., Dennison, C.A., Holmans, P., Walters, J.T.R., O'Donovan, M.C., and Owen, M.J. (2022). Ultrarare coding variants and cognitive function in schizophrenia. JAMA Psychiatry *79*, 963–970.

40. Nuechterlein, K.H., Green, M.F., Kern, R.S., Baade, L.E., Barch, D.M., Cohen, J.D., Essock, S., Fenton, W.S., Frese, F.J., 3rd, Gold, J.M., et al. (2008). The MATRICS Consensus Cognitive Battery, part 1: test selection, reliability, and validity. Am. J. Psychiatry *165*, 203–213.

41. Mesholam-Gately, R.I., Giuliano, A.J., Goff, K.P., Faraone, S.V., and Seidman, L.J. (2009). Neurocognition in first-episode schizophrenia: a meta-analytic review. Neuropsychology *23*, 315–336.

42. Minshew, N.J., Goldstein, G., and Siegel, D.J. (1997). Neuropsychologic functioning in autism: profile of a complex information processing disorder. J. Int. Neuropsychol. Soc. *3*, 303–316.

43. Hill, E.L. (2004). Executive dysfunction in autism. Trends Cogn. Sci. *8*, 26–32.

44. Palmer, D.S., Howrigan, D.P., Chapman, S.B., Adolfsson, R., Bass, N., Blackwood, D., Boks, M.P.M., Chen, C.-Y., Churchhouse, C., Corvin, A.P., et al. (2022). Exome sequencing in bipolar disorder identifies AKAP11 as a risk gene shared with schizophrenia. Nat. Genet. *54*, 541–547.

45. Kaplanis, J., Samocha, K.E., Wiel, L., Zhang, Z., Arvai, K.J., Eberhardt, R.Y., Gallone, G., Lelieveld, S.H., Martin, H.C., McRae, J.F., et al. (2020). Evidence for 28 genetic disorders discovered by combining healthcare and research data. Nature *586*, 757–762.

46. Karczewski, K.J., Francioli, L.C., Tiao, G., Cummings, B.B., Alföldi, J., Wang, Q., Collins, R.L., Laricchia, K.M., Ganna, A., Birnbaum, D.P., et al. (2020). The mutational constraint spectrum quantified from variation in 141,456 humans. Nature *581*, 434–443.

47. Aleman, A., and Kahn, R. (2005). Strange feelings: Do amygdala abnormalities dysregulate the emotional brain in schizophrenia? Prog. Neurobiol. *77*, 283–298.

48. Baron-Cohen, S., Ring, H.A., Bullmore, E.T., Wheelwright, S., Ashwin, C., and Williams, S.C. (2000). The amygdala theory of autism. Neurosci. Biobehav. Rev. *24*, 355–364.

49. Banker, S.M., Gu, X., Schiller, D., and Foss-Feig, J.H. (2021). Hippocampal contributions to social and cognitive deficits in autism spectrum disorder. Trends Neurosci. *44*, 793–807.

50. Lieberman, J.A., Girgis, R.R., Brucato, G., Moore, H., Provenzano, F., Kegeles, L., Javitt, D., Kantrowitz, J., Wall, M.M., Corcoran, C.M., et al. (2018). Hippocampal dysfunction in the pathophysiology of schizophrenia: a selective review and hypothesis for early detection and intervention. Mol. Psychiatry *23*, 1764–1772.

51. Zierhut, K., Bogerts, B., Schott, B., Fenker, D., Walter, M., Albrecht, D., Steiner, J., Schütze, H., Northoff, G., Düzel, E., et al. (2010). The role of hippocampus dysfunction in deficient memory encoding and positive symptoms in schizophrenia. Psychiatry Res. *183*, 187–194.

52. Moberg, S., and Takahashi, N. (2022). Neocortical layer 5 subclasses: From cellular properties to roles in behavior. Front. Synaptic Neurosci. *14*, 1006773.

53. Jutla, A., Foss-Feig, J., and Veenstra-VanderWeele, J. (2022). Autism spectrum disorder and schizophrenia: An updated conceptual review. Autism Res. *15*, 384–412.

54. Chang, J., Gilman, S.R., Chiang, A.H., Sanders, S.J., and Vitkup, D. (2015). Genotype to phenotype relationships in autism spectrum disorders. Nat. Neurosci. *18*, 191–198.

55. Peça, J., Feliciano, C., Ting, J.T., Wang, W., Wells, M.F., Venkatraman, T.N., Lascola, C.D., Fu, Z., and Feng, G. (2011). Shank3 mutant mice display autistic-like behaviours and striatal dysfunction. Nature *472*, 437–442.

56. Rothwell, P.E., Fuccillo, M.V., Maxeiner, S., Hayton, S.J., Gokce, O., Lim, B.K., Fowler, S.C., Malenka, R.C., and Südhof, T.C. (2014). Autism-associated neuroligin-3 mutations commonly impair striatal circuits to boost repetitive behaviors. Cell *158*, 198–212.

57. Chen, C.-Y., Tian, R., Ge, T., Lam, M., Sanchez-Andrade, G., Singh, T., Urpa, L., Liu, J.Z., Sanderson, M., Rowley, C., et al. (2023). The impact of rare protein coding genetic variation on adult cognitive function. Nat. Genet. *55*, 927–938.

58. Satterstrom, F.K., Kosmicki, J.A., Wang, J., Breen, M.S., De Rubeis, S., An, J.-Y., Peng, M., Collins, R., Grove, J., Klei, L., et al. (2020). Large-Scale Exome Sequencing Study Implicates Both Developmental and Functional Changes in the Neurobiology of Autism. Cell *180*, 568-584.e23.

59. Kepecs, A., and Fishell, G. (2014). Interneuron cell types are fit to function. Nature *505*, 318–326.

60. Chamberland, S., and Topolnik, L. (2012). Inhibitory control of hippocampal inhibitory neurons. Front. Neurosci. *0*, 165.

61. Letzkus, J.J., Wolff, S.B.E., and Lüthi, A. (2015). Disinhibition, a circuit mechanism for associative learning and memory. Neuron *88*, 264–276.

62. Pfeffer, C.K., Xue, M., He, M., Huang, Z.J., and Scanziani, M. (2013). Inhibition of inhibition in visual cortex: the logic of connections between molecularly distinct interneurons. Nat. Neurosci. *16*, 1068–1076.

63. Fu, Y., Tucciarone, J.M., Espinosa, J.S., Sheng, N., Darcy, D.P., Nicoll, R.A., and Stryker M (2014). A cortical circuit for gain control by behavioral state. Cell *156*, 1139–1152.

64. Bennett, C., Arroyo, S., Berns, D., and Hestrin, S. (2012). Mechanisms generating dual-component nicotinic EPSCs in cortical interneurons. J. Neurosci. *32*, 17287–17296.

65. Letzkus, J.J., Wolff, S.B.E., Meyer, E.M.M., Tovote, P., Courtin, J., Herry, C., and Lüthi, A. (2011). A disinhibitory microcircuit for associative fear learning in the auditory cortex. Nature *480*, 331–335.

66. Poorthuis, R.B., Enke, L., and Letzkus, J.J. (2014). Cholinergic circuit modulation through differential recruitment of neocortical interneuron types during behaviour: Cholinergic circuit modulation via interneurons. J. Physiol. *592*, 4155–4164.

67. Froemke, R.C., Merzenich, M.M., and Schreiner, C.E. (2007). A synaptic memory trace for cortical receptive field plasticity. Nature *450*, 425–429.

68. Lee, A.T., Cunniff, M.M., See, J.Z., Wilke, S.A., Luongo, F.J., Ellwood, I.T., Ponnavolu, S., and Sohal, V.S. (2019). VIP interneurons contribute to avoidance behavior by regulating information flow across hippocampal-prefrontal networks. Neuron *102*, 1223-1234.e4.

69. Marshall, C.R., Howrigan, D.P., Merico, D., Thiruvahindrapuram, B., Wu, W., Greer, D.S., Antaki, D., Shetty, A., Holmans, P.A., Pinto, D., et al. (2017). Contribution of copy number variants to schizophrenia from a genome-wide study of 41,321 subjects. Nat. Genet. *49*, 27–35.

70. Matsunami, N., Hadley, D., Hensel, C.H., Christensen, G.B., Kim, C., Frackelton, E., Thomas, K., da Silva, R.P., Stevens, J., Baird, L., et al. (2013). Identification of rare recurrent copy number variants in high-risk autism families and their prevalence in a large ASD population. PLoS One *8*, e52239.

71. Robin, N.H., and Shprintzen, R.J. (2005). Defining the clinical spectrum of deletion 22q11.2. J. Pediatr. *147*, 90–96.

72. Tang, K.L., Antshel, K.M., Fremont, W.P., and Kates, W.R. (2015). Behavioral and psychiatric phenotypes in 22q11.2 deletion syndrome. J. Dev. Behav. Pediatr. *36*, 639–650.

73. Swillen, A., Devriendt, K., Legius, E., Eyskens, B., Dumoulin, M., Gewillig, M., and Fryns, J.P. (1997). Intelligence and psychosocial adjustment in velocardiofacial syndrome: a study of 37 children and adolescents with VCFS. J. Med. Genet. *34*, 453–458.

74. Stark, K.L., Xu, B., Bagchi, A., Lai, W.S., Liu, H., Hsu, R., Wan, X., Pavlidis, P., Mills, A.A., Karayiorgou, M., et al. (2008). Altered brain microRNA biogenesis contributes to phenotypic deficits in a 22q11-deletion mouse model. Nat. Genet. *40*, 751–760.

75. Drew, L.J., Stark, K.L., Fénelon, K., Karayiorgou, M., Macdermott, A.B., and Gogos, J.A. (2011). Evidence for altered hippocampal function in a mouse model of the human 22q11.2 microdeletion. Mol. Cell. Neurosci. *47*, 293–305.

76. Zaremba, J.D., Diamantopoulou, A., Danielson, N.B., Grosmark, A.D., Kaifosh, P.W., Bowler, J.C., Liao, Z., Sparks, F.T., Gogos, J.A., and Losonczy, A. (2017). Impaired hippocampal place cell dynamics in a mouse model of the 22q11.2 deletion. Nat. Neurosci. *20*, 1612–1623.

77. Sun, Z., Williams, D.J., Xu, B., and Gogos, J.A. (2018). Altered function and maturation of primary cortical neurons from a 22q11.2 deletion mouse model of schizophrenia. Transl. Psychiatry *8*. https://doi.org/10.1038/s41398-018-0132-8.

78. Geiller, T., Vancura, B., Terada, S., Troullinou, E., Chavlis, S., Tsagkatakis, G., Tsakalides, P., Ócsai, K., Poirazi, P., Rózsa, B.J., et al. (2020). Large-Scale 3D Two-Photon Imaging of

Molecularly Identified CA1 Interneuron Dynamics in Behaving Mice. Neuron *108*, 968-983.e9.

79. Szalay, G., Judák, L., Katona, G., Ócsai, K., Juhász, G., Veress, M., Szadai, Z., Fehér, A., Tompa, T., Chiovini, B., et al. (2016). Fast 3D imaging of spine, dendritic, and neuronal assemblies in behaving animals. Neuron *92*, 723–738.

80. Katona, G., Szalay, G., Maák, P., Kaszás, A., Veress, M., Hillier, D., Chiovini, B., Vizi, E.S., Roska, B., and Rózsa, B. (2012). Fast two-photon in vivo imaging with three-dimensional random-access scanning in large tissue volumes. Nat. Methods *9*, 201–208.

81. Vancura, B., Geiller, T., Grosmark, A., Zhao, V., and Losonczy, A. (2023). Inhibitory control of sharp-wave ripple duration during learning in hippocampal recurrent networks. Nat. Neurosci. *26*, 788–797.

82. Somogyi, P., and Klausberger, T. (2005). Defined types of cortical interneurone structure space and spike timing in the hippocampus. J. Physiol. *562*, 9–26.

83. Guet-McCreight, A., Skinner, F.K., and Topolnik, L. (2020). Common principles in functional organization of VIP/calretinin cell-driven disinhibitory circuits across cortical areas. Front. Neural Circuits *14*, 32.

84. Varga, C., Golshani, P., and Soltesz, I. (2012). Frequency-invariant temporal ordering of interneuronal discharges during hippocampal oscillations in awake mice. Proc. Natl. Acad. Sci. U. S. A. *109*, E2726-34.

85. Lapray, D., Lasztoczi, B., Lagler, M., Viney, T.J., Katona, L., Valenti, O., Hartwich, K., Borhegyi, Z., Somogyi, P., and Klausberger, T. (2012). Behavior-dependent specialization of identified hippocampal interneurons. Nat. Neurosci. *15*, 1265–1271.

86. Katona, L., Lapray, D., Viney, T.J., Oulhaj, A., Borhegyi, Z., Micklem, B.R., Klausberger, T., and Somogyi, P. (2014). Sleep and movement differentiates actions of two types of somatostatin-expressing GABAergic interneuron in rat hippocampus. Neuron *82*, 872–886.

87. Somogyi, P., Katona, L., Klausberger, T., Lasztóczi, B., and Viney, T.J. (2014). Temporal redistribution of inhibition over neuronal subcellular domains underlies state-dependent rhythmic change of excitability in the hippocampus. Philos. Trans. R. Soc. Lond. B Biol. Sci. *369*, 20120518.

88. Turi, G.F., Li, W.-K., Chavlis, S., Pandi, I., Hare, J.O., Priestley, J.B., Grosmark, A.D., Liao, Z., Ladow, M., Zhang, J.F., et al. (2019). Vasoactive Intestinal Polypeptide-Expressing Interneurons in the Hippocampus Support Goal- Article Vasoactive Intestinal Polypeptide-Expressing Interneurons in the Hippocampus Support Goal-Oriented Spatial Learning. Neuron, 1–16.

89. Dudok, B., Klein, P.M., Hwaun, E., Lee, B.R., Yao, Z., Fong, O., Bowler, J.C., Terada, S., Sparks, F.T., Szabo, G.G., et al. (2021). Alternating sources of perisomatic inhibition during behavior. Neuron *109*, 997-1012.e9.

90. Friedrich, J., Zhou, P., and Paninski, L. (2017). Fast online deconvolution of calcium imaging data. PLoS Comput. Biol. *13*, e1005423.

91. Buzsáki, G., and Moser, E.I. (2013). Memory, navigation and theta rhythm in the hippocampal-entorhinal system. Nature Neuroscience 2013 16:2 *16*, 130–138.

92. O'Keefe, J., and Dostrovsky, J. (1971). The hippocampus as a spatial map. Preliminary evidence from unit activity in the freely-moving rat. Brain Res. *34*, 171–175.

93. Robinson, E.B., Samocha, K.E., Kosmicki, J.A., McGrath, L., Neale, B.M., Perlis, R.H., and Daly, M.J. (2014). Autism spectrum disorder severity reflects the average contribution of de novo and familial influences. Proc. Natl. Acad. Sci. U. S. A. *111*, 15161–15165.

94. Gonzalez-Burgos, G., and Lewis, D.A. (2012). NMDA receptor hypofunction, parvalbumin-positive neurons, and cortical gamma oscillations in schizophrenia. Schizophr. Bull. *38*, 950–957.

95. Buzsáki, G., and Draguhn, A. (2004). Neuronal oscillations in cortical networks. Science *304*, 1926–1929.

96. Van Derveer, A.B., Bastos, G., Ferrell, A.D., Gallimore, C.G., Greene, M.L., Holmes, J.T., Kubricka, V., Ross, J.M., and Hamm, J.P. (2021). A role for somatostatin-positive interneurons in neuro-oscillatory and information processing deficits in schizophrenia. Schizophr. Bull. *47*, 1385–1398.

97. Batiuk, M.Y., Tyler, T., Dragicevic, K., Mei, S., Rydbirk, R., Petukhov, V., Deviatiiarov, R., Sedmak, D., Frank, E., Feher, V., et al. (2022). Upper cortical layer-driven network impairment in schizophrenia. Sci. Adv. *8*, eabn8367.

98. Savage, J.E., Jansen, P.R., Stringer, S., Watanabe, K., Bryois, J., de Leeuw, C.A., Nagel, M., Awasthi, S., Barr, P.B., Coleman, J.R.I., et al. (2018). Genome-wide association meta-analysis in 269,867 individuals identifies new genetic and functional links to intelligence. Nat. Genet. *50*, 912–919.

99. Goff, K.M., and Goldberg, E.M. (2021). A role for vasoactive intestinal peptide interneurons in neurodevelopmental disorders. Dev. Neurosci. *43*, 168–180.

100. Mossner, J.M., Batista-Brito, R., Pant, R., and Cardin, J.A. (2020). Developmental loss of MeCP2 from VIP interneurons impairs cortical function and behavior. Elife *9*. https://doi.org/10.7554/eLife.55639.

101. Goff, K.M., Liebergall, S.R., Jiang, E., Somarowthu, A., and Goldberg, E.M. (2023). VIP interneuron impairment promotes in vivo circuit dysfunction and autism-related behaviors in Dravet syndrome. Cell Rep. *42*, 112628.

102. Luo, X., Guet-McCreight, A., Villette, V., Francavilla, R., Marino, B., Chamberland, S., Skinner, F.K., and Topolnik, L. (2020). Synaptic mechanisms underlying the network state-dependent recruitment of VIP-expressing interneurons in the CA1 hippocampus. Cereb. Cortex *30*, 3667–3685.

103. Kamigaki, T., and Dan, Y. (2017). Delay activity of specific prefrontal interneuron subtypes modulates memory-guided behavior. Nat. Neurosci. *20*, 854–863.

104. Möhler, H., and Rudolph, U. (2017). Disinhibition, an emerging pharmacology of learning and memory. F1000Res. *6*, 101.

105. Lovett-Barron, M., and Losonczy, A. (2014). Behavioral consequences of GABAergic neuronal diversity. Curr. Opin. Neurobiol. *26*, 27–33.

106. Murray, J.D., Anticevic, A., Gancsos, M., Ichinose, M., Corlett, P.R., Krystal, J.H., and Wang, X.-J. (2014). Linking microcircuit dysfunction to cognitive impairment: effects of disinhibition associated with schizophrenia in a cortical working memory model. Cereb. Cortex *24*, 859–872.

107. Ioannidis, N.M., Rothstein, J.H., Pejaver, V., Middha, S., McDonnell, S.K., Baheti, S., Musolf, A., Li, Q., Holzinger, E., Karyadi, D., et al. (2016). REVEL: An Ensemble Method for Predicting the Pathogenicity of Rare Missense Variants. Am. J. Hum. Genet. *99*, 877–885.

108. Samocha, K.E., Kosmicki, J.A., Karczewski, K.J., O'Donnell-Luria, A.H., Pierce-Hoffman, E., MacArthur, D.G., Neale, B.M., and Daly, M.J. (2017). Regional missense constraint improves variant deleteriousness prediction. bioRxiv, 148353. https://doi.org/10.1101/148353.

109. SPARK https://sparkforautism.org/.

110. Chiang, A.H., Chang, J., Wang, J., and Vitkup, D. (2021). Exons as units of phenotypic impact for truncating mutations in autism. Mol. Psychiatry *26*, 1685–1695.

111. Lovett-Barron, M., Kaifosh, P., Kheirbek, M.A., Danielson, N., Zaremba, J.D., Reardon, T.R., Turi, G.F., Hen, R., Zemelman, B.V., and Losonczy, A. (2014). Dendritic inhibition in the hippocampus supports fear learning. Science *343*, 857–863.

112. Acsády, L., Görcs, T.J., and Freund, T.F. (1996). Different populations of vasoactive intestinal polypeptide-immunoreactive interneurons are specialized to control pyramidal cells or interneurons in the hippocampus. Neuroscience *73*, 317–334.

113. Acsády, L., Arabadzisz, D., and Freund, T.F. (1996). Correlated morphological and neurochemical features identify different subsets of vasoactive intestinal polypeptide-immunoreactive interneurons in rat hippocampus. Neuroscience *73*, 299–315.

114. Tyan, L., Chamberland, S., Magnin, E., Camiré, O., Francavilla, R., David, L.S., Deisseroth, K., and Topolnik, L. (2014). Dendritic inhibition provided by interneuron-specific cells controls the firing rate and timing of the hippocampal feedback inhibitory circuitry. J. Neurosci. *34*, 4534–4547.

115. Pelkey, K.A., Chittajallu, R., Craig, M.T., Tricoire, L., Wester, J.C., and Mcbain, X.C.J. (2017). Hippocampal GABAergic inhibitory interneurons. Physiol. Rev. *97*, 1619–1747.

116. Francavilla, R., Villette, V., Luo, X., Chamberland, S., Muñoz-Pino, E., Camiré, O., Wagner, K., Kis, V., Somogyi, P., and Topolnik, L. (2018). Connectivity and network state-dependent recruitment of long-range VIP-GABAergic neurons in the mouse hippocampus. Nat. Commun. *9*, 5043.

117. Kaifosh, P., Zaremba, J.D., Danielson, N.B., and Losonczy, A. (2014). SIMA: Python software for analysis of dynamic fluorescence imaging data. Front. Neuroinform. *8*, 80.

118. Kang, H.J., Kawasawa, Y.I., Cheng, F., Zhu, Y., Xu, X., Li, M., Sousa, A.M.M., Pletikos, M., Meyer, K.A., Sedmak, G., et al. (2011). Spatio-temporal transcriptome of the human brain. Nature *478*, 483–489.